Journal of Sound and Vibration 618 (2025) 119336

Contents lists available at ScienceDirect

Journal of Sound and Vibration

journal homepage: www.elsevier.com/locate/jsvi

The effect of the leading-edge separation bubble vortex shedding on the far field noise of a Controlled Diffusion airfoil: A DNS study

Andrea Arroyo Ramo [a,b,*], Stéphane Moreau [a], Richard D. Sandberg [c], Michaël Bauerheim [b], Marc C. Jacob [d]

[a] Université de Sherbrooke, Mechanical Engineering, Canada
[b] ISAE-SUPAERO, Département Aérodynamique, Énergétique et Propulsion, France
[c] University of Melbourne, Department of Mechanical Engineering, Victoria, Australia
[d] École Centrale de Lyon, Laboratoire de Mécanique des Fluides et d'Acoustique, France

ARTICLE INFO

Keywords:
Aeroacoustics
Airfoil noise
Direct numerical simulation
Separation bubble
Compressible flow
Acoustic propagation

ABSTRACT

A Direct Numerical Simulation (DNS) of the compressible flow and the near-field acoustics has been achieved over a Controlled Diffusion (CD) airfoil embedded in the core of an open-jet wind tunnel at a geometrical angle of attack of 8°, a Reynolds number based on the chord $Re = 1.5 \times 10^5$, and a Mach number $M = 0.25$ to investigate the turbulent flow field and the associated noise generation mechanisms. The non-uniform boundary conditions computed previously by a RANS calculation provide the mean installation effects. The mesh topology consists of a new chimera approach with overlapping meshes. To obtain the far-field noise prediction, the DNS has been coupled with both the Ffowcs Williams and Hawkings acoustic analogy and Amiet's model. The new DNS results have been first validated against detailed experimental data and prior DNS with multi-block body-fitted topology. They then identify and estimate three noise sources: (i) the interaction between the attached turbulent flow and the airfoil trailing edge, (ii) the laminar separation bubble (LSB) at the suction side leading edge, and (iii) a source in the near wake. The latter two contribute mainly at high frequencies, and their directivity is identified for the first time. Moreover, the separation and reattachment noise generation by the suction side LSB of a CD airfoil is demonstrated, confirming a previous experimental conjecture. In addition, the work takes advantage of the high-quality dataset generated to carry out a novel investigation on the airfoil pressure side.

1. Introduction

Noise pollution is a general concern as it produces negative effects on human and animal health. The noise emitted by turbomachines found in our daily life such as cooling fans, air conditioning units, wind turbines, or propellers is then becoming the target of more stringent regulations, and therefore must be reduced. In rotating machines, the blade self-noise is an important contributor to the total noise emitted, and is responsible for the minimum noise level produced by these machines [1,2]. Its origin is the interaction of the turbulent eddies born in the boundary layer and wake unsteadiness with the airfoil itself [3]. In most cases, noise is generated as the turbulent eddies of the boundary layer are convected past the trailing edge, where they get significantly distorted, converting the vorticity modes into acoustic waves. In the case of a blunt – rounded – trailing edge, and when the local boundary layer thickness does not exceed a certain fraction of the trailing edge thickness, vortices may periodically form in the very

* Corresponding author at: Université de Sherbrooke, Mechanical Engineering, Canada.
E-mail addresses: andrea.arroyo.ramo@usherbrooke.ca, andrea.arroyoramo@gmail.com (A. Arroyo Ramo).

https://doi.org/10.1016/j.jsv.2025.119336
Received 2 October 2024; Received in revised form 9 July 2025; Accepted 11 July 2025
Available online 5 August 2025

near wake, yielding some additional vortex shedding noise [4]. The resulting aerodynamic pressure fluctuations on the airfoil are scattered into tones or narrowband humps by the trailing edge. Additional airfoil tonal noise caused by laminar boundary instability noise has also been reported [5–7]. However, in the present study, tonal noise mechanisms will not be addressed. The focus will be on the broadband noise generated by the interaction of the turbulent flow with the airfoil surface, usually occurring at the trailing edge. Note that in both cases, the main scattering process is a more efficient noise mechanism than collisions of turbulent eddies in free space at low Mach numbers.

Because of the complex nature of the physical mechanisms underlying the trailing-edge noise, several approaches have been introduced over time for its prediction. Most of the models are based on the pioneering theoretical work of Ffowcs Williams and Hall [8], Amiet [9], and Howe [10]. All of them assume the airfoil to be a semi-infinite flat plate, ignoring the finite chord and thickness of the airfoil, as well as its curvature. Whereas the model of Ffowcs Williams and Hall requires the determination of a quadrupolar source term, Amiet's model relies on the unsteady pressure response on the airfoil surface assumed as equivalent dipoles into Curle's acoustic analogy [11]. Amiet's theory has been recurrently used as an approach to predict self-noise, as it relates the far-field acoustic pressure to the wall-pressure statistics upstream of the trailing edge [12]. It assumes a frozen turbulence stream, where the turbulent velocity field is not affected by the location of the airfoil edge. The frozen turbulence is convected past the trailing edge, and allows estimating the pressure discontinuity as a perturbation of the upstream boundary layer pressure field. Roger and Moreau [13–15] extended Amiet's theory to include the leading-edge back-scattering effect. In the case of studying curved surfaces – airfoils –, as the wall-pressure field is modified along the streamwise direction, the unperturbed wall-pressure field is usually estimated at 95%–98% of the chord. Finally, the far-field sound noise spectrum is predicted from the wall-pressure statistics, which can be obtained either from experiments or analytical models or numerical simulations.

In the last decade, detailed unsteady compressible numerical simulations, such as Large Eddy Simulations (LES) [16–18], and Direct Numerical Simulations (DNS) [17,19–24], have been used to predict trailing-edge noise, often by combining the high-fidelity simulations with a Ffowcs Williams and Hawkings (FWH) acoustic analogy to predict the far field noise. To reduce the required computational resources, the direct computation of the noise is performed only in the near field, and then, it is propagated to the far field using a lower-cost approach. In this way, the associated highly-demanding discretization requirements are limited to the region around the airfoil, and not needed in the complete domain. This hybrid process allows identifying all self-noise sources, validating the simplifying assumptions that are introduced in the analytical models introduced previously, and extending them if required.

The present work deals with the numerical study of the Controlled Diffusion (CD) airfoil. It is a thin-cambered airfoil (4 % thickness and 12° camber angle) used in several industrial applications (e.g., turbo-engine compressor and fan blades, automotive engine cooling fans, etc.) because of its capability of reducing aerodynamic losses. The CD airfoil has been broadly studied in low Reynolds number flows and at low Mach numbers, either experimentally or numerically [7,18,21–32]. Usually, in simulations, the airfoil is immersed in a uniform unperturbed flow. However, when trailing-edge noise experiments are performed in an open-jet anechoic wind tunnel, the airfoil is immersed in a non-uniform potential core of the jet. Thus, compared with free field configurations, these open-jet configurations exhibit significant installation effects that modify both the flow field around the airfoil and the sound field [33]. In particular, the boundary layer development and separation on the airfoil [21] are altered. The influence can be so strong that the experimental wind tunnel configuration should be accounted for when comparing numerical and experimental data. For this reason, in the present study, a DNS of the CD airfoil accounting for the installation effects is thus carried out. The boundary conditions are inhomogeneous, in order to match the experimental open-jet configuration. As for the earliest trailing-edge noise predictions based on incompressible LES [28,34–36], a Reynolds-Averaged Navier–Stokes (RANS) simulation of the wind-tunnel two-dimensional section has been employed to obtain these mean boundary conditions. The main objective of this work is to investigate in detail the turbulent flow field and its associated broadband self-noise generation in the vicinity of the airfoil with a new Chimera-type grid topology. The airfoil is immersed in the open-jet potential core at an angle of incidence of 8°, a Reynolds number based on the chord $Re = 1.5 \times 10^5$, and a Mach number $M = 0.25$. This configuration allows the study of low-speed fan systems, and their noise sources. To verify that the flow behavior is properly represented, these simulations are compared with experimental data under equivalent conditions, as well as with previous multi-block body-fitted DNS including installation effects [23]. An exhaustive study on the wall-pressure statistics has been performed for the first time on both the suction and pressure sides of the airfoil, particularly around the laminar separation bubble (LSB) that develops near the leading edge. It has allowed the noise sources mechanism to be evaluated. Finally, in order to predict the resulting far-field noise, the approaches of FW-H and Amiet's are applied and their outputs are compared. A complete analysis of the near-field and far-field acoustic propagation is also achieved for the first time, noticeably the contributions of the three identified noise sources to the directivity.

2. Numerical modeling

2.1. Flow-field model

The full dimensionless compressible Navier–Stokes equations (continuity, momentum, and energy conservation) govern both the flow and the sound field around the CD airfoil, the underlying system of equations is:

$$\frac{\partial \rho}{\partial t} + \frac{\partial}{\partial x_j}\left(\rho u_j\right) = 0 \tag{1}$$

$$\frac{\partial}{\partial t}\left(\rho u_i\right) + \frac{\partial}{\partial x_j}\left[\rho u_i u_j + p\delta_{ij} - \tau_{ij}\right] = 0 \tag{2}$$

$$\frac{\partial}{\partial t}(\rho E) + \frac{\partial}{\partial x_j}\left[\rho u_j \left(E + \frac{p}{\rho}\right) + q_j - u_k \tau_{kj}\right] = 0 \tag{3}$$

where ρ is the density, u_i stands for the i velocity component, p is the pressure, and δ_{ij} is the Kronecker symbol. Under the assumption of Newtonian fluid and ideal gas, the total energy E is defined, together with the molecular stress tensor τ_{ij}, and heat flux vector q_i as follows:

$$E = \frac{T}{\gamma(\gamma-1)M^2} + \frac{u_k u_k}{2} \tag{4}$$

$$\tau_{ij} = \frac{\mu}{Re}\left(\frac{\partial u_i}{\partial x_j} + \frac{\partial u_j}{\partial x_i} - \frac{2}{3}\frac{\partial u_k}{\partial x_k}\delta_{ij}\right) \tag{5}$$

$$q_i = \frac{-1}{(\gamma-1)M^2}\frac{\mu}{RePr}\frac{\partial T}{\partial x_i} \tag{6}$$

where Pr stands for the Prandtl number (constant value of $Pr = 0.72$), $\gamma = 1.4$ is the heat capacity ratio, and the dynamic viscosity μ is computed from the Sutherland's law (Eq. (7)), with $T_s = 291.15$ K, $\mu_s = 1.716 \times 10^{-5}$ Pa.s and $C_s = 110.4$ K. Finally, to close the system of equations, the state equation is used, where $R = 287.05$ J.kg^{-1}K^{-1}.

$$\mu = \mu_s \left(\frac{T}{T_s}\right)^{3/2} \frac{T_s + C_s}{T + C_s} \tag{7}$$

$$p = \rho R T \tag{8}$$

2.2. Numerical solver and flow topology

The numerical code to perform the current simulations is *HiPSTAR* (High Performance Solver for Turbulence and Acoustic Research) [37]. It resolves the aforementioned N-S equations in dimensionless form, using as reference values the airfoil chord length, and the free-stream velocity, density, and temperature to obtain the equivalent system of equations [38]. This code is a low-dissipative-low-dispersive program which uses a 4th-order central standard-difference accurate scheme with Carpenter boundary stencils in the x-y plane (streamwise and cross-stream directions) to ensure the 4th-order precision at the boundaries of the domain [39]. In the spanwise direction, a high-order spectral method based on the FFTW3 library is used for discretization.

In contrast to the work of Wu et al. [22,23], in which these authors performed a DNS on the CD airfoil using a multi-block body-fitted structured domain, in the present study, a multi-block overset structured grid [40] is employed. The main advantage of this mesh topology is its flexibility when performing airfoil rotations to evaluate multiple angles of incidence, and different boundary conditions induced by different jet widths, for instance. In the current case, the domain is divided into two overlapping structured grids, which are independent of each other: the background mesh (Block 1) and the O-grid mesh (Block 2) (see Fig. 1(a)). The O-grid mesh can be arbitrarily rotated to simulate any angle of incidence. At the interface between both blocks, the solution is interpolated from the matching points of the mesh blocks that overlap. The first block (background), consists of 1800 × 1000 evenly-spaced grid points along the x and y directions respectively. The second block (O-grid) surrounds the airfoil (see Fig. 1(b)). This second mesh type allows controlling the refinement regions around the airfoil, by clustering the largest amount of points near the wall, and in the neighborhood of the leading and trailing edges of the airfoil, as depicted in Figs. 1(c) and 1(d). A total of 1000 × 140 grid points are found in the x-y plane of Block 2.

In the spanwise direction, the extent of the domain is $0.1\,c$, which was proven to be sufficiently large for the considered flow conditions [27,28]. A previous study of grid sensitivity was performed in which the spanwise resolution was varied from 32 to 96 spanwise spectral modes to discretize the spanwise extent [41]. Grid convergence was achieved for all integral quantities (boundary-layer thicknesses, pressure, and friction coefficients) and wall-pressure statistics with 96 modes. The number of spectral modes used in this study is therefore 96, or 194 collocation points, which translates into an overall of about 186 million points in the three-dimensional domain. The mesh resolution of the DNS case is evaluated by means of the dimensionless grid sizes at the wall, which is shown in Fig. 2. The values in the wall-normal directions are $y^+ < 1$ for most of the airfoil surface (below 0.75 in the whole turbulent region on the suction side), which correspond to commonly agreed values for DNS resolution [42,43]. In Fig. 2(b) the grid resolution study of the spanwise modes evidences the decrease of z^+ as the spanwise modes increase, to reach values below 10 in the entire turbulent region for 96 modes only. The wall-streamswise direction is $x^+ < 30$ in the whole domain.

The time marching of the solver is achieved by an ultra-low storage 4th-order accurate five-stage Runge–Kutta integration scheme [44]. To ensure the stability of the computation, the non-dimensional time step is set to 1.5×10^{-5}, which is equivalent to a physical time step of 1.27×10^{-7} s. This time-step produces a CFL < 1 in the domain, ensuring the stability of the computation. Its maximum value in the whole domain is $\mathrm{CFL}_{\max} = 0.9976$ in Block 2 (O-grid mesh), close to the airfoil leading edge. To provide an order of magnitude of the computational cost of the DNS, running on 64 parallel GPUs has required about 27 khGPU to complete.

2.3. Initial and boundary conditions

The flow conditions in which the CD airfoil is immersed in the current computations are a geometrical angle of attack $\alpha = 8°$, a chord-based Reynolds number $Re = 1.5 \times 10^5$, and a Mach number $M = 0.25$. To reproduce the experimental conditions, the influence of the installation effects is considered, as it modifies the airfoil loading [23]. The boundary conditions of the current DNS aim to mimic the characteristics of the wind tunnel found at Ecole Centrale de Lyon (ECL) and Université de Sherbrooke (UdeS). They

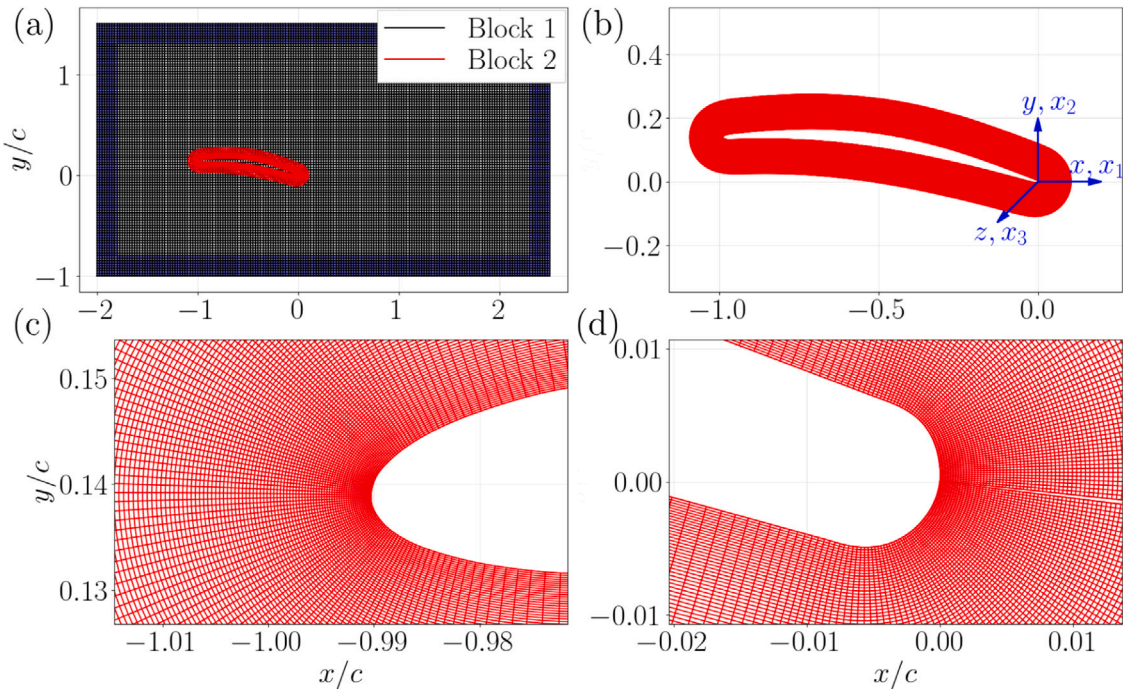

Fig. 1. DNS mesh. Two overlapping blocks composing the domain: background and O-grid mesh. 2D-spanwise slicing-cut representation of the mesh. Spanwise homogeneous extrusion to obtain the 3D volume mesh. (a) Complete domain, showing only every 10 grid lines and the outer rectangular sponges. (b) O-grid meshing details, with Amiet's reference coordinate system. Origin at trailing edge. (c) and (d) Leading and trailing edge meshing details, respectively.

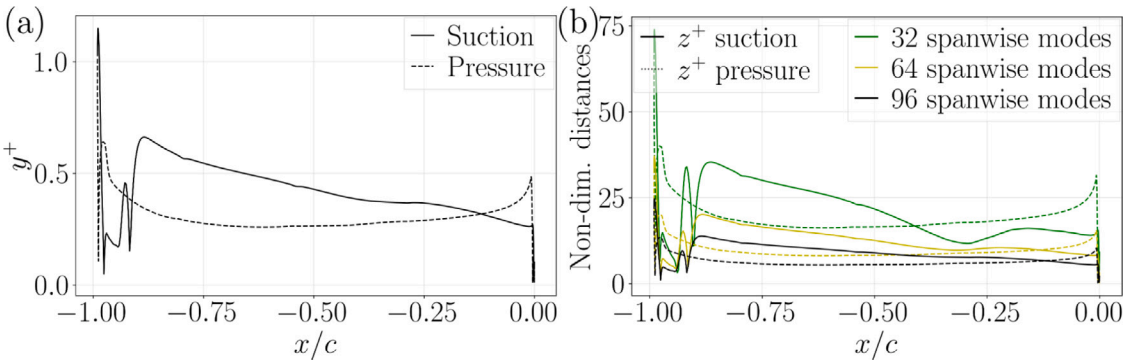

Fig. 2. Non-dimensional wall distances. (a) Wall-normal distance. (b) Spanwise distances, spanwise convergence.

include the flow deflection that occurs in the core of the 50 cm jet in the wind tunnel. To include such effects in the simulation, a 2D RANS solution of the flow around the CD airfoil has been first computed, similarly to what was applied before for incompressible airfoil LES [28,34–36]. This RANS accounts for the 2D experimental geometric configuration, including the jet nozzle [21] (see Fig. 3). In the RANS calculation, the turbulence model employed is the k-ω SST, as it agrees well with the experimental velocity field and the laminar recirculation bubble on the CD airfoil [33].

The computational domain is shown in Fig. 3. It is such that the DNS domain is located within the jet potential core. Special attention has been paid to the boundaries of the domain to prevent spurious/nonphysical reflections, as well as to impose the corresponding mean velocity profiles resulting from the RANS calculations. A buffer region is included upstream of the physical domain with the aim of damping any upstream traveling flow perturbations before reaching the boundary and producing undesired reflecting waves. Downstream, a Zonal Characteristic Boundary Condition is applied [45] to ramp towards zero the characteristics before reaching the end of the domain (see the rectangular regions next to the boundaries in Fig. 1(a)). Finally, at the airfoil surface, a no-slip condition is applied. The steps to include the initial and boundary conditions in the DNS calculations are described in more detail in [46].

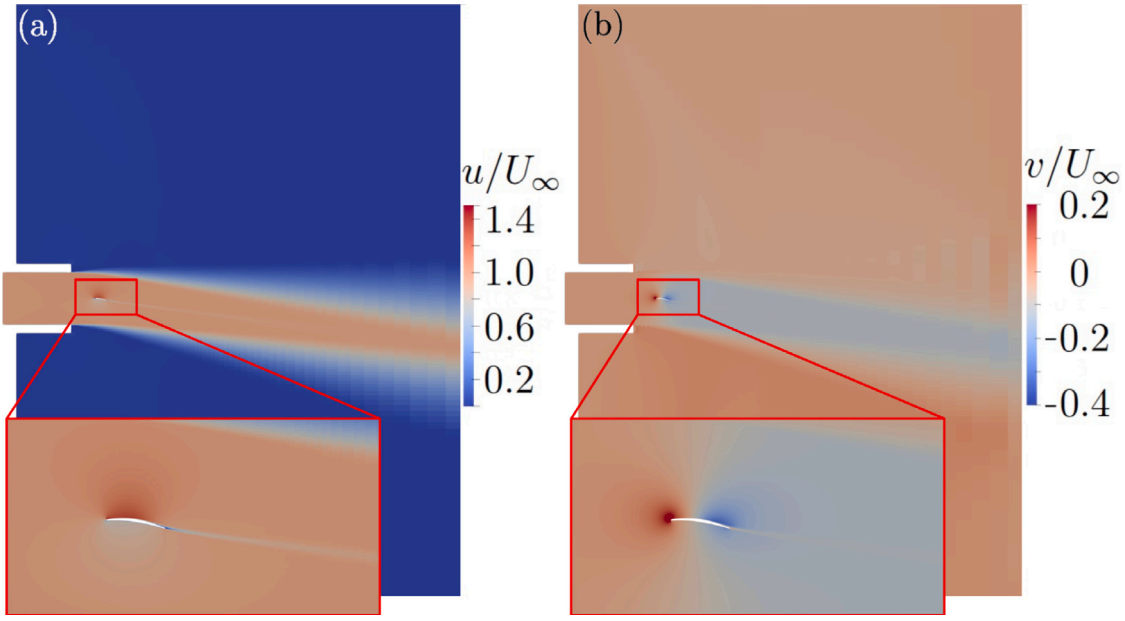

Fig. 3. Velocity contours of the 2D RANS calculation employed as initialization values for DNS computation. DNS domain delimited by the rectangle, and zoomed-in to show the details near the airfoil. (a) and (b) x and y velocity components, respectively.

2.4. Far-field acoustic post-processing

In this work, two acoustic propagation approaches have been employed to investigate the acoustic radiation of the CD airfoil: Amiet's model and Ffowcs-Williams and Hawkings' acoustic analogy. The former considers trailing-edge noise diffraction only, while the latter identifies all possible noise sources on the airfoil.

2.4.1. Amiet's model

The first approach used in this work to perform acoustic predictions is Amiet's analytical trailing-edge noise model [9] and its extension [13,14]. It has been developed to account for the contribution of trailing-edge noise to the overall airfoil noise production. The principle is the following one: the turbulent flow upstream of the trailing edge produces a pressure field, which is decomposed into gusts that are convected towards the trailing edge using a Fourier Transform. Near the trailing edge, these pressure gusts scatter into a radiating acoustic pressure field. The observer coordinates are defined as x_1, x_2 and x_3 (streamwise, cross-stream, and spanwise coordinates respectively, as seen in Fig. 1(b)). The axial and spanwise coordinates of the infinitely thin flat plate that replaces the CD airfoil in the model are y_1 and y_3 respectively. If the airfoil span d is assumed to be large, the power spectral density (PSD) of the far-field acoustic pressure S_{pp} at an observer located in the $x_3 = 0$ plane is given by

$$S_{pp}(x_1, x_2, 0, \omega) = \left(\frac{\omega b x_2}{2\pi c_0 \sigma^2}\right)^2 l_{y_3}(\omega) d |\mathscr{L}(x_1, K_x)|^2 \phi_{pp}(\omega, 0) \tag{9}$$

with ω the angular frequency, c_0 the sound speed, and K_x the convective wave number. The other parameters are defined as $\sigma^2 = x_1^2 + \beta^2\left(x_2^2 + x_3^2\right)$, $\beta^2 = 1 - M^2$ where M is the Mach number. The spanwise coherence length $l_{y_3}(\omega)$ is defined as

$$l_{y_3}(\omega) = \frac{1}{\phi_{pp}(\omega, 0)} \int_0^\infty \left|\phi_{pp}\left(\omega, y_3\right)\right| \, \mathrm{d}y_3 \tag{10}$$

and can be approximated by $l_{y_3}(\omega) = 2.1 U_c/\omega$ for a turbulent boundary layer in a uniform flow with no mean pressure gradient, where U_c is the convection speed. The PSD of the wall-pressure fluctuations $\phi_{pp}(\omega, 0)$ can be extracted from the experimental data. In this work, it is estimated from the DNS results. It can also be approximated with empirical expressions proposed for turbulent boundary layers. In particular, the non-dimensional frozen power spectrum $\phi_{pp}(\omega, 0)$ is expressed by Lee's [47] extension of Rozenberg's model [48] as:

$$\frac{\phi(\omega) U_e}{\tau_w^2 \delta^*} = \frac{\max\left(a, \left(0.25\beta_c - 0.52\right) a\right) \left(\omega\delta^*/U_e\right)^2}{\left[4.76\left(\omega\delta^*/U_e\right)^{0.75} + d^*\right]^e + \left[8.8 R_T^{-0.57}\left(\omega\delta^*/U_e\right)\right]^{h^*}} \tag{11}$$

where τ_w is the wall-shear stress, $\beta_c = (\theta/\tau_w)/(\partial p/\partial x)$ the Clauser parameter, and $R_T = (\delta/U_e)/(\nu/u_\tau^2) = (u_\tau \delta/\nu)\sqrt{C_f/2}$ the inner-to-outer time scales. The parameters a to h define characteristics of the wall-pressure spectrum: $a = 2.28\Delta^2(6.13\Delta^{-0.75} + d)^e(4.2\Pi/\Delta + 1)$,

$d^* = \max(1, 1.5d)$, $d = 4.76(1.4/\Delta)^{0.75} \cdot (0.375e - 1)$, $e = 3.7 + 1.5\beta_c$, and $h^* = \min(3, (0.139 + 3.1043\beta_c)) + 7$, the wake strength parameter $\Pi = 0.8(\beta_c + 0.5)^{3/4}$, and Zaragola and Smits's parameter $\Delta = \delta/\delta^*$.

To complete Amiet's model, the radiation integral in Eq. (9), $|\mathscr{L}(x_1, K_x)|$, which can be derived analytically, includes the main scattering from the trailing-edge and the back-scattering from the leading edge [13–15].

2.4.2. Ffowcs williams and hawkings's acoustic analogy

In the second approach for the acoustic propagation, the DNS calculations are coupled with an in-house Ffowcs Williams and Hawkings (FWH) solver – *SherFWH* – in order to obtain the acoustic radiation from the CD airfoil. *SherFWH* is meant to compute the far-field acoustic pressure from the near-field pressure provided by the DNS. The FWH acoustic analogy requires enclosing the sound sources with a control surface. In the present case, as the solid formulation of the FWH approach is employed, the control surface is the wall of the airfoil, where the spatial resolution is the finest. The data that feed the acoustic solver are recorded at a sampling frequency of 78.6 kHz. The acoustic signature at any observer position, for the solid formulation of FWH is obtained from the following equation:

$$p'(\mathbf{x}, t) = \underbrace{\frac{\partial}{\partial t} \int_{f=0} \left[\frac{Q_i n_i}{4\pi |\mathbf{x} - \mathbf{y}|} \right]_{\tau_e} \mathrm{d}S}_{\text{Thickness noise (monopole)}} - \underbrace{\frac{\partial}{\partial x_i} \int_{f=0} \left[\frac{L_{ij} n_j}{4\pi |\mathbf{x} - \mathbf{y}|} \right]_{\tau_e} \mathrm{d}S}_{\text{Loading noise (dipole)}} \tag{12}$$

In the case of a permeable control surface, the source terms Q_i, L_{ij} write:

$$Q_i = \rho \left(u_i - v_i \right) + \rho_0 v_i \tag{13}$$

$$L_{ij} = \rho u_i \left(u_j - v_j \right) + \left(p - p_0 \right) \delta_{ij} - \sigma_{ij} \tag{14}$$

where u_i and v_i are the flow velocity at the surface and the surface velocity, respectively. Their difference vanishes in the case of a solid surface, leaving: $Q_i = \rho_0 v_i$ and $L_{ij} = (p - p_0)\delta_{ij} - \sigma_{ij}$. The control surface enclosing the sound sources is represented by $f(\mathbf{x}, t) = f = 0$, and $[]_{\tau_e}$ denotes the evaluation at the emission time τ_e.

Two main terms compose the far-field acoustic pressure at this low Mach number: the monopolar and the dipolar terms, which correspond to the thickness and loading noise, respectively. The locations of the numerical microphone arrays in the far field are such that both the variation of the noise radiation with distance to the trailing edge and its directivity can be evaluated. Indeed, both a circumferential and radial arrays yield the sound directivity and its decay rate with increasing distance (Fig. 3 in [46]).

3. Results

The DNS results are compared to experimental and numerical data when available. The airfoil mock-up shown in Fig. 4 is instrumented with remote microphone probes (RMP), the locations of which are collected in Table 1 [49].

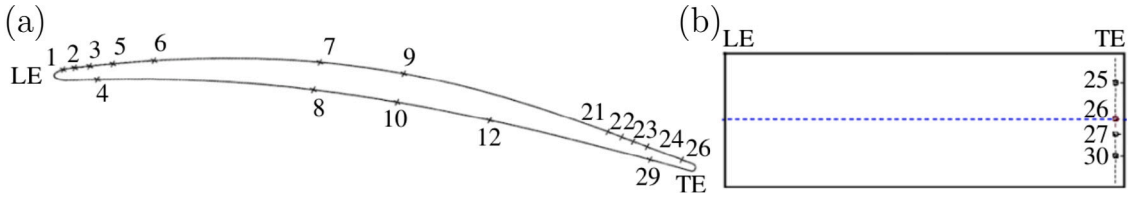

Fig. 4. Remote microphone probe location on the airfoil surface. (a) Side view. (b) Top view.

Table 1
Remote microphone probe locations.

Suction side leading edge to midchord	RMP	1	2	3	5	6	7	9	
	x/c	0.011	0.022	0.045	0.077	0.146	0.404	0.533	
	z/c	0.05	0.05	0.05	0.05	0.05	0.05	0.05	
Suction side trailing edge	RMP	21	22	23	24	25	26	27	30
	x/c	0.858	0.878	0.899	0.916	0.973	0.973	0.973	0.973
	z/c	0.05	0.05	0.05	0.05	0.013	0.05	0.065	0.087
Pressure side	RMP	4		8		10		29	
	x/c	0.067		0.321		0.4630		0.934	
	z/c	0.05		0.05		0.05		0.05	

3.1. Instantaneous flow field

In Fig. 5, the instantaneous field of the Q-criterion (second invariant of the velocity gradient tensor) is colored by the streamwise velocity u. The main focus is on the leading and trailing-edge regions. An LSB is found at the leading edge of the suction side, (see Fig. 5(a)). Large coherent structures are shed from the LSB, and trigger the transition from laminar to turbulent flow on the suction side.

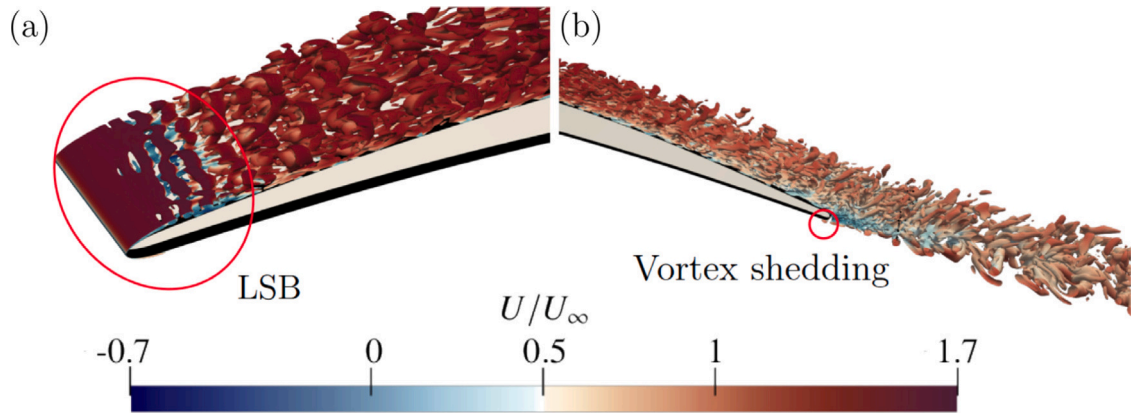

Fig. 5. Instantaneous field of Q-criterion colored by u velocity component on the airfoil surface. (a) and (b) Leading and trailing edge details, respectively.

Moving towards the trailing edge (see Fig. 5(b)), the flow is nearly attached along the airfoil surface. As previously reported, on the pressure side, the transition to turbulence occurs close to the trailing edge, where some vortex shedding occurs. The present instantaneous flow field Q-criterion iso-contours (Q = 250) agrees with the one reported by Wu et al. [50] with the swirling strength criterion with $\lambda_{ci} = 70$.

3.2. Mean flow

3.2.1. Wall-pressure and friction coefficients

The wall-pressure distribution on the airfoil is used to evaluate the installation effects. The time and spanwise averaged wall-pressure coefficient is defined as

$$C_p = \frac{\langle p \rangle - p_\infty}{1/2\,\rho_\infty\,U_\infty^2} \tag{15}$$

with $\langle p \rangle$ the time and spanwise averaged wall-pressure distribution, and p_∞, ρ_∞, and U_∞ the free-stream pressure, density and velocity, respectively. All mean-flow statistics are computed by averaging over the 194 collocation points used in the spanwise direction The results are compared in Fig. 6(a) with experimental data from the Université de Sherbrooke (UdeS), Ecole Centrale de Lyon (ECL), Delft University of Technology (TU Delft) and Michigan State University (MSU), and with numerical data of DNS carried out by Wu et al. [23], which also includes the installation effects. On the one hand, the flow on the pressure side is characterized by a Favorable Pressure Gradient (FPG). It is fully laminar up to the trailing edge, where it mixes with the flow coming from the suction side. On the other hand, the suction side presents several complex physical processes. At the leading edge, the plateau that covers about 10% of the chord corresponds to the Laminar Separation Bubble (LSB). This effect is more pronounced (larger LSB extension) in the simulations compared to the experiments because of the lack of residual background turbulence in the simulations [51]. At ECL and Michigan State University (MSU), the inlet turbulence intensity ranged from 0.8% to 1.0%, and at UdeS and TU-Delft it was below 0.4%. The slight difference between the two DNS in the LSB is most likely caused by the slight variation of jet deflection shown in Appendix. After the flow re-attachment and the laminar-to-turbulent transition at about 10% chord, a mild FPG zone develops up to mid-chord followed by a growing Adverse Pressure Gradient (APG) region, which thickens the turbulent boundary layer that remains attached up to the trailing edge.

The friction coefficient on the airfoil surface is shown in Fig. 6(b). The time and spanwise averaged wall-friction coefficient is defined as

$$C_f = \frac{\langle \tau_w \rangle}{1/2\,\rho_\infty\,U_\infty^2} \tag{16}$$

with $\langle \tau_w \rangle$ the time and spanwise averaged wall shear stress $\tau_w = \mu \left(\frac{\partial U}{\partial y} \right)_{y=0}$. The present results show good agreement with Wu's DNS data in Fig. 6(b). On the suction side, the LSB produces a recirculation region responsible for negative values of C_f. The end of the LSB is determined by the position where C_f changes sign, which happens around $x/c = -0.9$ (10% chord). This agrees with the plateau found in Fig. 6(a). With increasing mean adverse pressure, C_f decreases but remains positive, confirming that the flow is attached up to the trailing edge.

3.2.2. Velocity profiles

The velocity profiles are evaluated both over the airfoil – suction and pressure sides – and in the near wake. They provide information on the aerodynamic features of the flow near the airfoil, and they allow validating the computations with previous

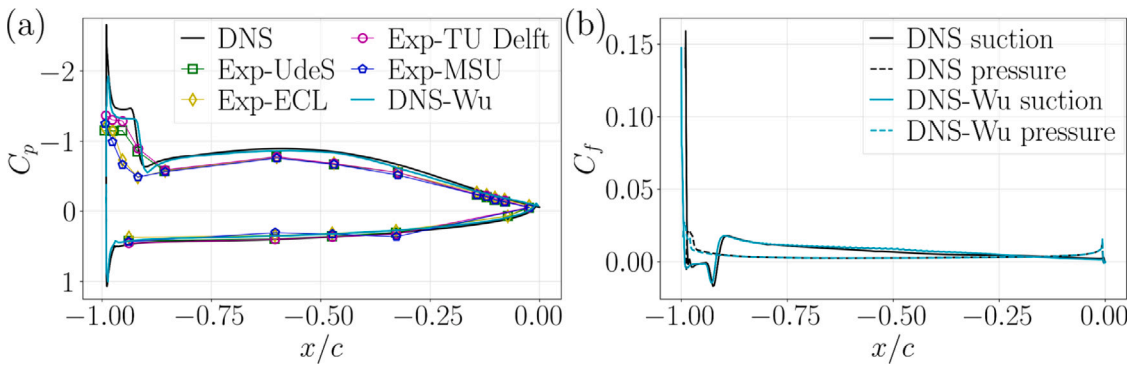

Fig. 6. Mean dimensionless coefficients. (a) Wall-pressure coefficient, C_p. (b) Wall-friction coefficient, C_f.

experimental and numerical data. The Hot Wire (HW) data comes from Michigan State University (MSU), and the Particle Image Velocimetry (PIV) is from UdeS [52].

The near-wall mean velocity profiles in Figs. 7 and 9 represent the evolution against the normal dimensionless distance-to-wall (h/c) of the tangential velocity U_t (velocity aligned with the airfoil surface) normalized by the maximum tangential velocity found in the velocity profile $U_{t,\max}$. The near-wake mean velocity profiles are normalized by the maximum value of the streamwise velocity component $U_{\max}$. To obtain the value of the edge velocity U_e, required to find the extent of the boundary layer, several steps are required. First, the boundary layer thickness must be computed. It is calculated based on the conservation of the stagnation pressure $p_t = \rho U_t^2/2 + p_\infty$ outside the boundary layer. At the edge of the boundary layer, the 95% recovery of the total pressure is used as the criterion to define the end of the boundary layer, as the edge velocity is not constant around the airfoil in the jet potential core [22,53].

The evolution of the mean velocity profiles on the suction side follows that of the wall coefficients in the previous section. RMP 3 is completely immersed inside the LSB. The negative values of the velocity are evidence of the recirculating region. At RMP 5, as in the experiment, the positive mean value of the tangential velocity shows that the end of the LSB is reached. Note that, in the previous DNS of Wu et al. [50], there is still a small recirculation region. The mid-chord region of RMPs 6 to 9 is characterized by almost Zero Pressure Gradients (ZPG) as the velocity profiles hardly evolve, and the boundary layer thickness remains almost constant as

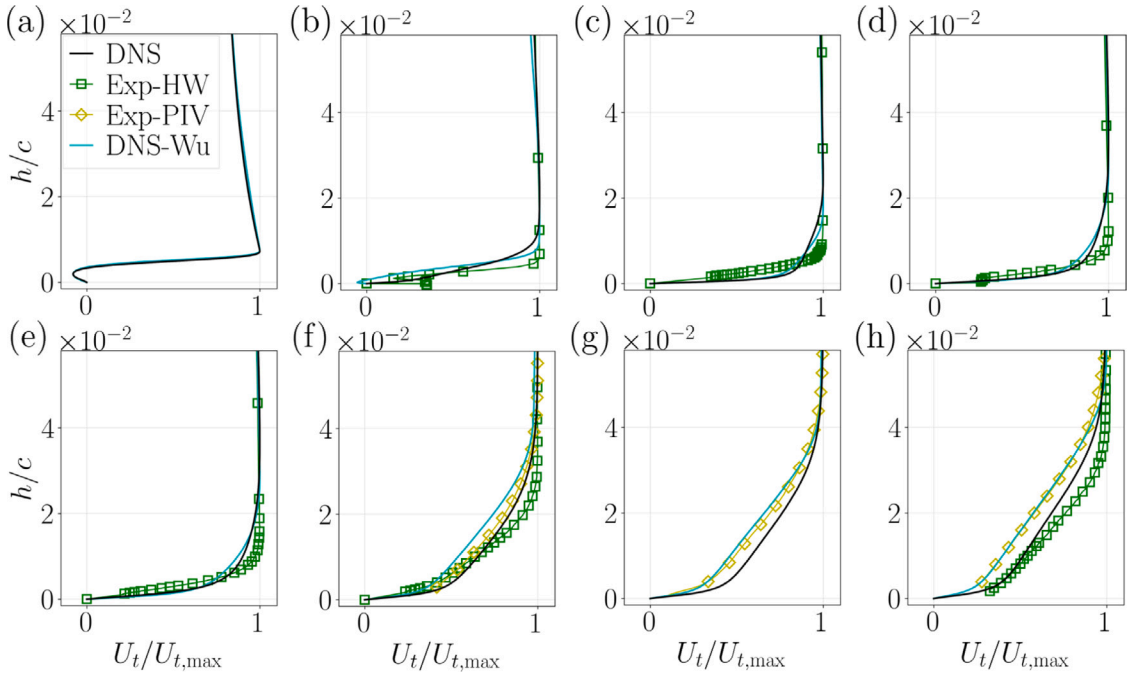

Fig. 7. Suction side mean velocity profiles at positions: (a) RMP 3, (b) RMP 5, (c) RMP 6, (d) RMP 7, (e) RMP 9, (f) RMP 21, (g) RMP 24, and (h) RMP 26. Comparison with experimental and DNS data extracted from Wu et al. [23]. Hot-wire experimental data from MSU and PIV experimental data from UdeS.

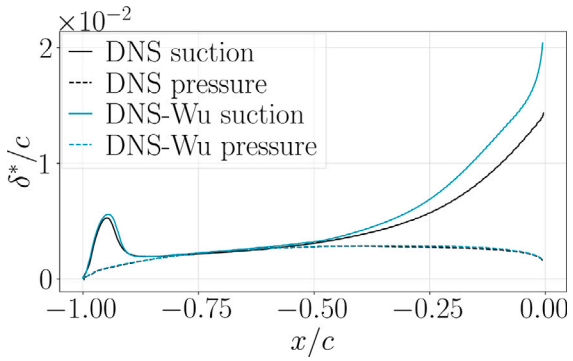

Fig. 8. Boundary layer displacement thickness. Comparative of DNS results.

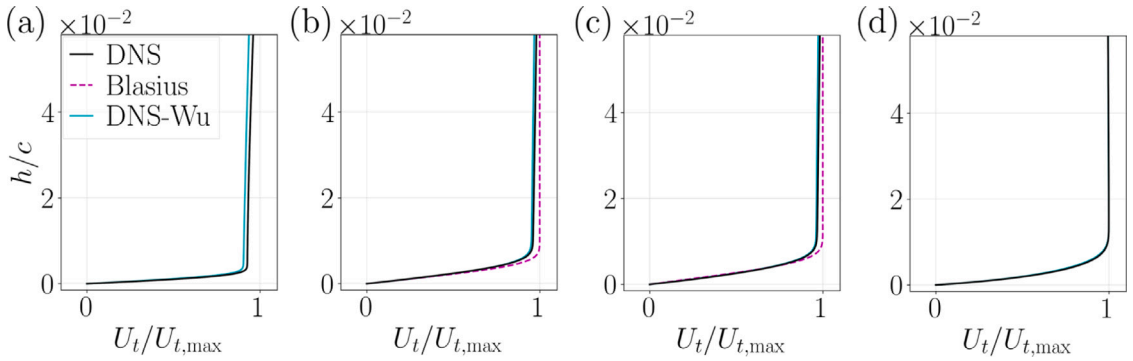

Fig. 9. Pressure side mean velocity profiles at positions: (a) RMP 4, (b) RMP 8, (c) RMP 10, and (d) RMP 29. Comparison with DNS data extracted from Wu et al. [23], and Blasius BL profile applied at RMPs 8 and 10.

previously reported by Caiazzo et al. (Figure 6 (a) in [54]). RMP 9 shows a good match between the numerical and experimental data. Close to the trailing edge, from RMPs 21 to 26, the APG becomes more and more important when approaching the trailing edge. Overall, there is a good match between the experimental data and the current mean values of the DNS cases. Moreover, the shape of the velocity profiles is well captured. Nevertheless, the boundary layer displacement thickness in Fig. 8 emphasizes the differences between the current and the previous DNS [22,23]. The size of the LSB is slightly larger in the previous DNS, as well as the boundary layer thickness in the farthest downstream 20% portion of the airfoil suction side. This different development of the turbulent boundary layer is again most likely caused by the slight different jet deflection induced by the inlet boundary conditions, as shown in Appendix.

The evolution of the mean velocity profiles on the pressure side also compares well with the result of the body-fitted DNS. Additionally, since RMPs 8 and 10 do not present any pressure gradient as illustrated in Fig. 6(a), the velocity profiles at the corresponding positions show a good match with the Blasius solution of the laminar boundary layer on a flat plate [55].

The velocity profiles have also been evaluated in the near wake. Both, mean and fluctuating root-mean-square (RMS) velocities in the x and y directions, respectively are shown in Figs. 10 and 11, respectively. The locations evaluating the near wake profiles are $x/c = 0.075$, 0.169, and 0.206. The mean velocity profile is also compared to the 2D RANS case of the full experimental set-up further downstream from the airfoil, at $x/c = 2$. The mean near-wake velocity profiles show an overall good agreement with both experimental and numerical data. At $x/c = 0.075$, the closest to the trailing edge, the profiles of the vertical velocity component v present a discrepancy of about 20% on the asymptotic external velocity. The 2D RANS velocity is also included in this comparison, and it seems that this shift in values is related to the RANS uncertainty on the velocity profiles imposed at the boundaries. This may imply a slight modification in the airfoil loading. However, when moving further downstream, the vertical velocity component is again in agreement with the experimental data. Thus, the uncertainty related to the RANS profiles is more pronounced in the vicinity of the airfoil. Furthermore, the minimum velocity on the midline of the wake deficit matches the experimental data well. The near wake deficit peak is almost aligned with the airfoil chord, at a geometrical angle of attack of 8°.

The RMSs of the fluctuating velocity profiles (see Fig. 11) show a good general agreement, particularly with the hot-wire measurements. There is some reduction of the peak amplitudes in the wake deficit, which might be caused by some smoothing introduced by the spatial interpolation, as a result of moving from the most refined mesh in the O-grid region towards the background mesh. Nevertheless, the results display that the present DNS computation provides a quite reliable fluctuating hydrodynamic field that should lead to a proper representation of the acoustic field.

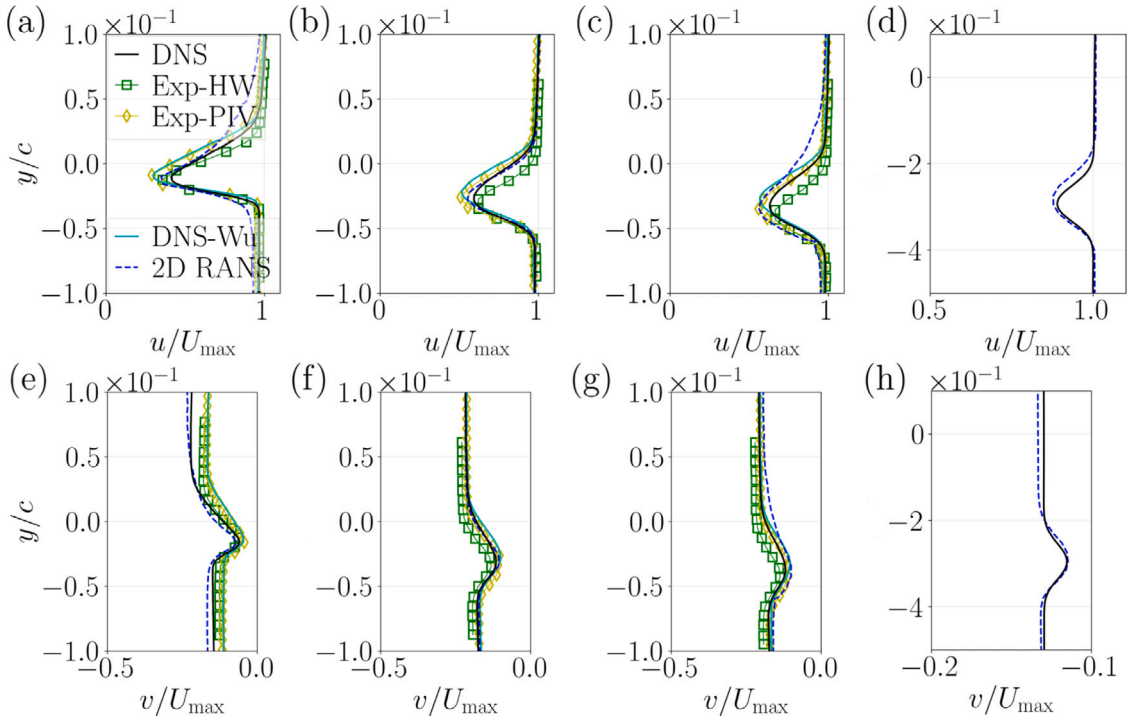

Fig. 10. Near-wake and wake mean velocity profiles. Horizontal and vertical velocity components downstream the trailing edge at locations: (a, e) $x/c = 0.075$, (b, f) $x/c = 0.169$, (c, g) $x/c = 0.206$, and (d, h) $x/c = 2$. Comparison with experimental, DNS data extracted from Wu et al. [23] and 2D RANS data used as initialization and boundaries in the current simulation.

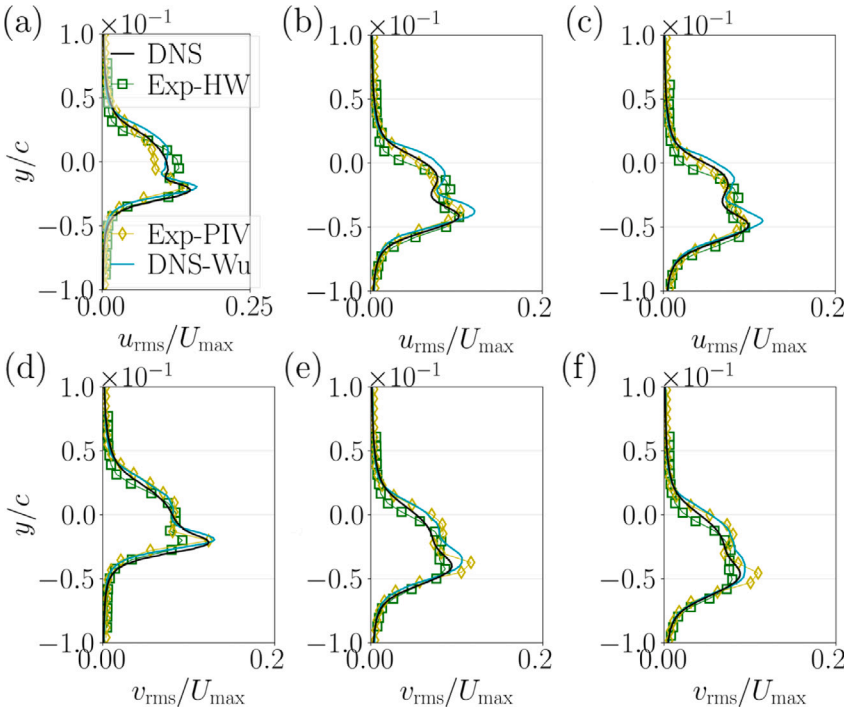

Fig. 11. Near-wake fluctuating velocity profiles. Horizontal and vertical velocity components downstream the trailing edge at locations: (a, (d) $x/c = 0.075$, (b, (e) $x/c = 0.169$, (c, (f) $x/c = 0.206$. Comparison with experimental and DNS data extracted from Wu et al. [23].

3.3. Wall-pressure statistics

The pressure signals have been recorded for 10 flow-through times, at a sampling frequency of about 78.6 kHz. The raw numerical data is scaled to obtain the corresponding dimensional quantities matching the experimental conditions. To do so, the dimensionless pressure is multiplied by the reference dynamic pressure $\rho_{\text{ref}}U_{\text{ref}}^2$. The wall-pressure statistics are computed for the sensors on the suction side in the FPG, ZPG and APG regions and compared with experimental and numerical data when available. Additional comparisons are provided on the pressure side with mild pressure gradients for the first time. At all RMP locations close to the trailing edge, the local pressure field has been found to be homogeneous in the planes across the spanwise extent [29], as well as stationary in time, once the flow is fully established.

The space–time cross-correlation function of the wall-pressure fluctuations $p' = p - \overline{p}$ for two points arbitrarily separated in space and time is defined as follows.

$$R_{pp}(\xi_x, \xi_z, \tau) = \lim_{T\to\infty} \frac{1}{T} \int_0^T p'(x, z, t)p'(x + \xi_x, z + \xi_z, t + \tau)\mathrm{d}t \tag{17}$$

In this case, since the statistics are computed at the wall, only the streamwise and spanwise separations (ξ_x, ξ_z) account for the space variation. The temporal variation is accounted for with the time delay τ. Then, the cross-spectral density (CSD) is defined as the Fourier transform of the cross-correlation:

$$\psi_{pp}(\xi_x, \xi_z, \omega) = \frac{1}{2\pi} \int_{-\infty}^{\infty} R_{pp}(\xi_x, \xi_z, \tau)e^{-\mathrm{i}\omega\tau}\mathrm{d}\tau, \tag{18}$$

and is computed by means of a Fast Fourier Transform (FFT) over time for the angular frequency ω using a Welch periodogram technique with 16 Hanning windows, 50% overlap and zero padding.

In order to obtain the single-point wall-pressure PSD (i.e. auto-spectrum), ϕ_{pp}, at a given angular frequency ω, the space–time cross correlation in Eq. (17) is evaluated with null space separation between points $(\xi_x = 0, \xi_z = 0)$, leading to:

$$\phi_{pp}(\omega) = \psi_{pp}(0, 0, \omega) = \frac{1}{2\pi} \int_{-\infty}^{\infty} R_{pp}(0, 0, \tau)e^{-\mathrm{i}\omega\tau}\mathrm{d}\tau \tag{19}$$

Finally, the cross-spectrum, together with the auto-spectrum, is useful to obtain the wall-pressure spatial coherence as a function of the frequency [27]. The coherence is defined as:

$$\gamma^2(\xi_x, \xi_z, \omega) = \frac{\left|\psi_{pp}(\xi_x, \xi_z, \omega)\right|^2}{\phi_{pp}(\omega)^2} \tag{20}$$

It provides the level of correlation between two points that are spatially separated at a given frequency. In the following sections, the wall-pressure statistics results of this work are presented.

3.3.1. PSD of the wall-pressure fluctuations

The suction side PSD of the wall-pressure fluctuations for RMPs 3, 5, 6, 7, 9, 21, 24 and 26 are shown in Fig. 12. The results are compared with experimental data of UdeS and MSU as well as with numerical DNS results when available. RMP 3 represents the location inside the LSB, and produces a hump in the spectral levels at about $5-6$ kHz, which matches the previous DNS numerical data and is also found experimentally at slightly higher frequencies.

The numerical results, as they provide a larger LSB, locate RMP 5 just after reattachment, which then still yields a wider and weaker hump in the range 5–6 kHz. In the experimental data, with a smaller bubble size, at RMP 5 where the flow is completely reattached, no more hump is observed. In the ZPG region, the results show a faster roll-off at high frequencies compared to Wu's DNS. This is mostly caused by the aforementioned different development of the turbulent boundary layer. Nevertheless, the current simulations are mostly in agreement with UdeS experiments at RMP 9. Moving towards the APG zone, the results exhibit a low-frequency range that fits well with the experimental data. At RMP 26, the closest to the trailing edge, an extra mild hump is observed at frequencies over 10 kHz (also seen in RMP 24). Note that the present mesh size in the chordwise direction at the aft positions of the airfoil surface yields a frequency resolution up to 25 kHz. The beginning of this hump can also be guessed in the UdeS measurements. In the case of Wu's simulation, the associated levels are larger than those found in the present simulation. This high-frequency hump was attributed to the acoustic imprint on the wall of an additional noise source in the wake [23]. The streamwise grid resolution being twice larger in the near wake in the present DNS most likely damps this additional secondary noise source, producing a plateau rather than a hump in the trailing-edge wall spectra. More details are provided in Appendix. Finally, Lee's model (dashed line) is computed at the trailing edge with the boundary layer parameters corresponding to RMP 26. It almost perfectly fits the experimental data as well as the present DNS up to $6-7$ kHz, although it does not provide any hint of the aforementioned high-frequency hump, as expected. This suggests that another physical mechanism than the classical trailing edge noise source governs the high frequency hump.

The pressure side PSD of the wall-pressure fluctuations are shown in Fig. 13. The four RMPs that are evaluated are 4, 8, 10, and 29. Because of the laminar nature of the flow along the entire pressure surface, the wall-pressure fluctuations have much lower levels than on the suction side (PSD about 20 dBs less) with a much faster roll-off around 1 kHz. Both DNS show similar low-frequencies levels, and exhibit a sharp increase of levels at about 4 kHz in the previous DNS and 4.6 kHz in the present one. Several sharp quasi-tonal peaks, harmonics of these initial frequencies, are then seen in both cases at high frequencies. This sudden increase in levels on all RMPs can only be attributed to acoustic waves moving through the laminar boundary layer. Note also that the broadband hump covers a zone from about 4 kHz to 20 kHz that corresponds to the frequency range of the humps seen on the suction side of the LSB (RMPs 3 and 5) and near the trailing edge (RMPs 24 and 26).

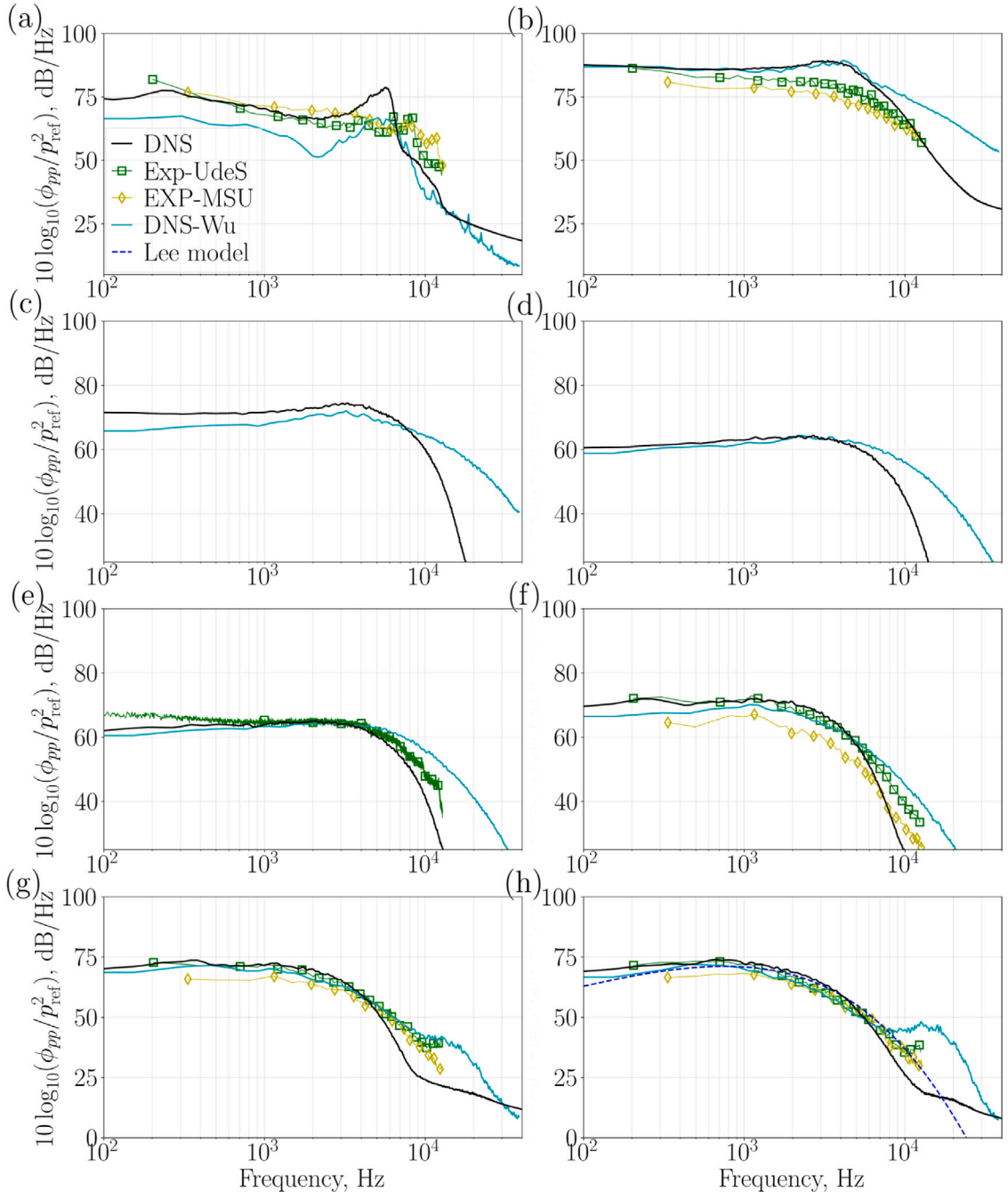

Fig. 12. Spanwise-averaged PSD of wall-pressure fluctuations on the suction side at positions: ((a) RMP 3, (b) RMP 5, (c) RMP 6, (d) RMP 7, (e) RMP 9, (f) RMP 21, (g) RMP 24, and (h) RMP 26. $P_{\mathrm{ref}} = 2 \times 10^{-5}$ Pa.

3.3.2. Two-point streamwise wall-pressure correlation and convection velocity

The space and time variations of the two-point correlation of the wall-pressure fluctuations at the suction side are shown in Fig. 14 as a function of the normalized streamwise and temporal separations. To normalize the streamwise separation ξ_x, the displacement thickness at probe 7 in the ZPG region is used as reference for all RMP locations ($\delta^*_{\mathrm{in}} = \delta^*_{\mathrm{RMP}\ 7}$). For normalization of the temporal separation, the edge velocity U_e at RMP 7 is used, together with the displacement thickness at probe 7 δ^*_{in}. The convection speed of the eddies is obtained by means of the slope $\mathrm{d}(\xi_x)/\mathrm{d}(\Delta t)$. This slope is calculated, both, by fitting the points joining the maximum

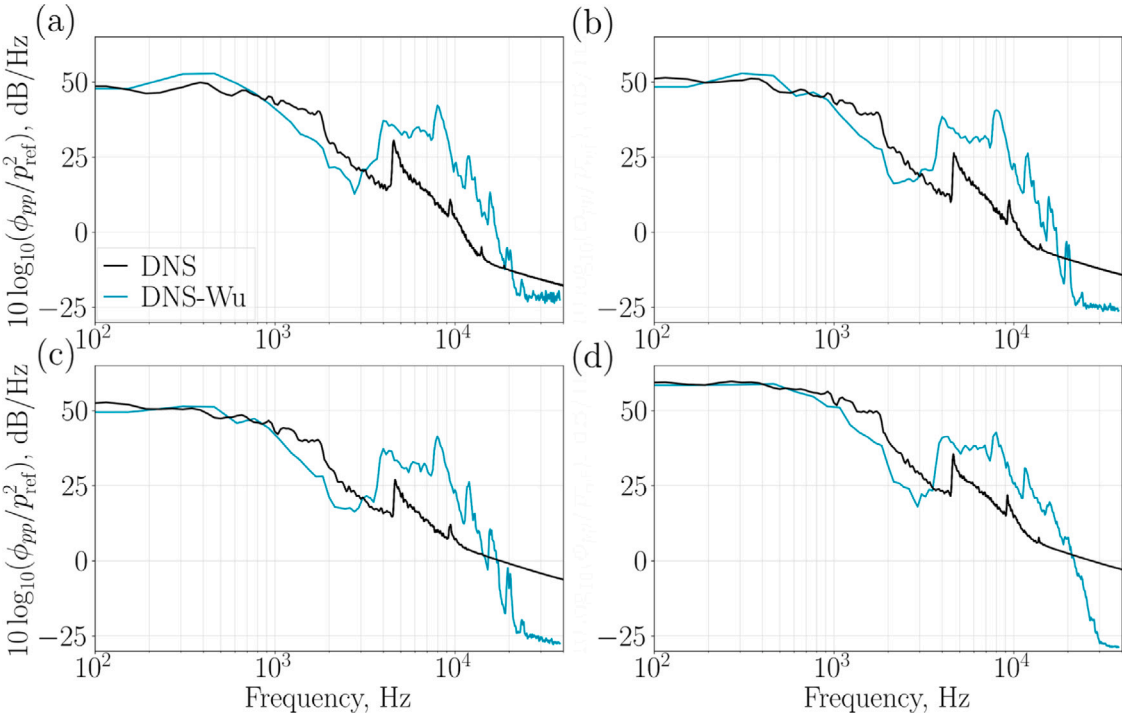

Fig. 13. Spanwise-averaged PSD of wall-pressure fluctuations on the pressure side at positions: (a) RMP 4, (b) RMP 8, (c) RMP 10, and (d) RMP 29. $P_{ref} = 2 \times 10^{-5}$ Pa.

values of the two-point correlation iso-contours, and by obtaining the slope $\mathrm{d}(\xi_x)/\mathrm{d}(\Delta t)$ at the origin of the coordinates, as explained by Caiazzo et al. [54].

At RMPs 3 and 5, the effect of the LSB is evidenced. Multiple correlated structures appear at the location of the RMP ($\xi_x/\delta^*_{in} = 0$). At RMP 5, since it is located at the very end of the recirculating region at the vicinity of the reattachment point, only a few secondary structures appear. At RMP 6, a secondary structure appears, as it corresponds to the correlation of the points upstream RMP 6 (in between RMPs 5 and 6). RMPs 7 and 9 are located in the ZPG region, and RMPs 21, 24 and 26 in the APG, with stronger APG effect when closer to the trailing edge. As expected, a larger propagation speed is observed in the ZPG region compared to the APG, where the convection of the turbulent structures is reduced. There is a variation in the size of large-scale structures as the pressure gradient varies, and the contour plot becomes broader as the APG effect increases, as shown by Caiazzo et al. [54]. The value of the convection speed for the ZPG and APG regions is collected in Table 2. The results agree with those found by Na and Moin [56], Schloemer [57] and Caiazzo et al. [54].

On the pressure side, the space–time variations of the two-point correlation of the wall-pressure fluctuation are also evaluated and collected in Fig. 15. The representation is such that the complete pressure side correlation is shown for each of the RMP locations, from the leading edge to the trailing edge, and setting $\xi_x/c = 0$ at the RMP position. The pressure field has been filtered around the first quasi-tonal peak frequency – 4.6 kHz – found in the PSD of the pressure side wall-pressure fluctuations (Fig. 13). Due to the laminar nature of the boundary layer, multiple correlated structures appear in a periodic fashion. The slope of the central structure has been used to obtain the convection speed at each location of the probe. The corresponding values are collected in Table 3. The local mean flow propagation and the relative perturbation speed are also gathered in the table. As deduced from the negative slope produced by the space–time correlation, disturbances travel upstream, going from the trailing edge towards the leading edge.

Table 2
Suction side convection velocity in Zero Pressure Gradient and Adverse Pressure Gradient sensors location.

	ZPG		APG		
RMP	7	9	21	24	26
DNS U_c/U_∞	[0.61 – 0.77]	[0.61 – 0.71]	[0.55 – 0.49]	[0.52 – 0.50]	[0.48 – 0.38]
DNS-Wu U_c/U_∞ Caiazzo et al. [54]	0.8		0.5		
Na and Moin U_c/U_∞ [56]	0.79		0.56		
Schloemer U_c/U_∞ [57]	0.75		0.54		

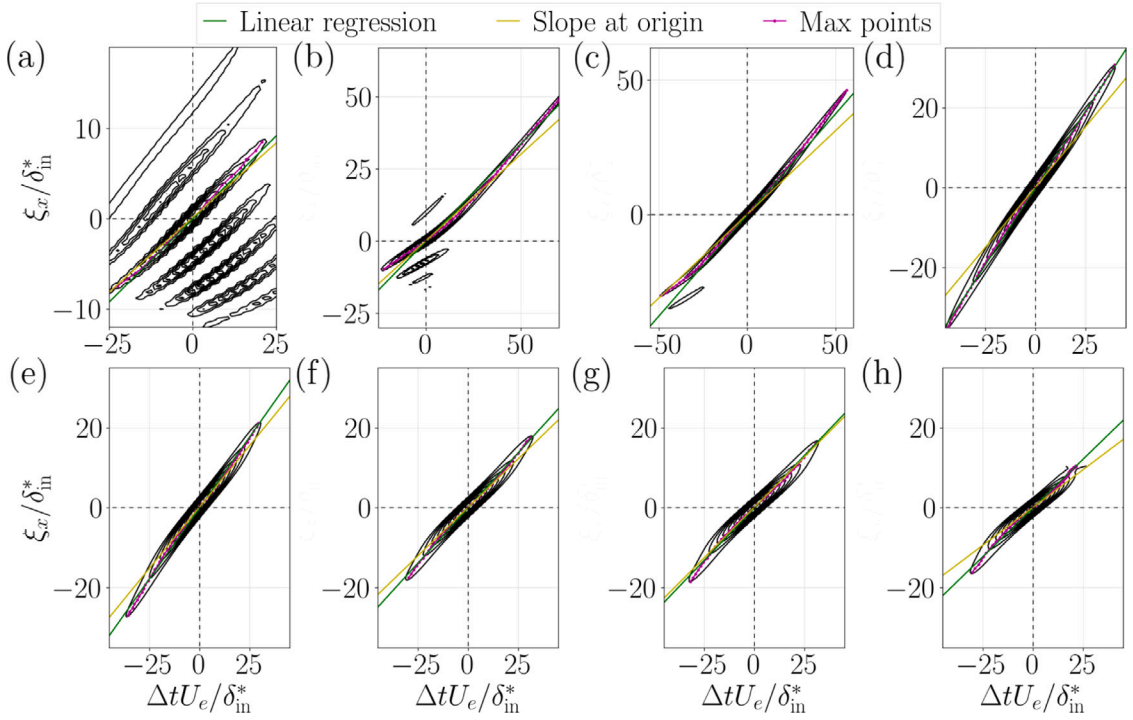

Fig. 14. Contours of two-point correlation of wall-pressure fluctuations at the suction side as a function of spatial and temporal separation. Positions: (a) RMP 3, (b) RMP 5, (c) RMP 6, (d) RMP 7, (e) RMP 9, (f) RMP 21, (g) RMP 24, and (h) RMP 26.

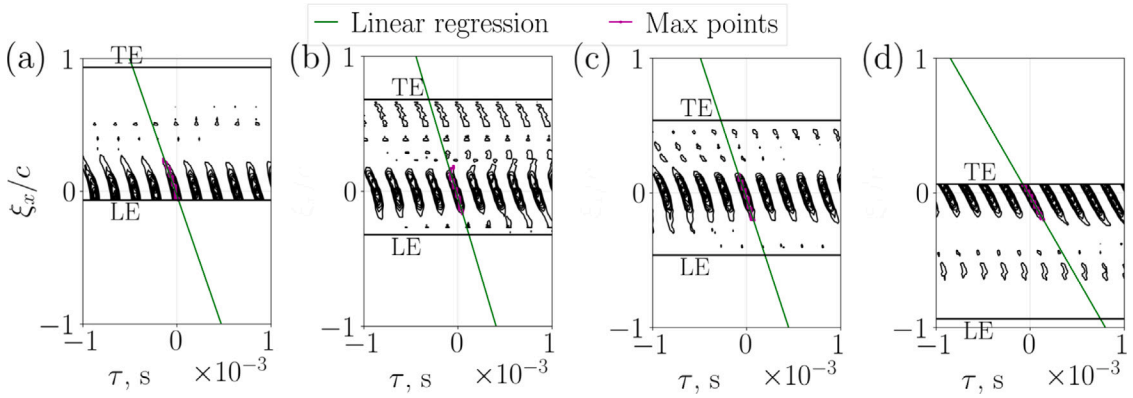

Fig. 15. Contours of two-point correlation of wall-pressure fluctuations at the pressure side as a function of spatial and temporal separation. Positions: (a) RMP 4, (b) RMP 8, (c) RMP 10, and (d) RMP 29.

Table 3
Pressure side local velocities.

RMP	4	8	10	29
Convection speed U_c (m/s)	−278.60	−318.40	−289.61	−164.51
Mean-flow propagation U_x (m/s)	12.95	12.98	13.16	14.91
Absolute perturbation speed (m/s)	−291.55	−331.38	−303.22	−179.42

To obtain the absolute perturbation speed, the mean-flow propagation has been considered. At RMPs 4, 8, and 10, the absolute perturbation speed is of the order of magnitude of the sound speed. Therefore, it is concluded that the quasi-tonal peaks are caused by acoustic waves moving through the laminar boundary layer from trailing edge towards leading edge. The reduced slope of the space–time correlation at RMP 29, hence reduced propagation speed, is most likely related to the local trailing-edge vortex shedding on the pressure side.

3.3.3. Wall-pressure coherence

The spanwise coherence of wall-pressure fluctuations evaluated close to the trailing edge (98% of the chord) in Fig. 16, compare well with that in [27]. This spanwise coherence is mainly significant at low frequencies below 1 kHz, as also noted by Wang et al. [28]. The three sensors undergo an exponential decay both in the experiments and in the DNS, similarly to Corcos' model [58] for a fully turbulent boundary layer. As expected in turbulent boundary layers, as the distance between RMPs 25, 27 and 30 increases with respect to RMP 26, from which the coherence has been computed, the spanwise coherence becomes lower.

The streamwise coherence of wall-pressure fluctuations is represented in Figs. 17(a) and 17(b) near the leading edge and the trailing edge, respectively, and compared with ECL experiment [27]. At low frequencies (up to 1 kHz), the highest values of coherence with RMP 5 are reached with RMPs 2, 3, and 6, while the rest of the sensors have almost no correlation. For these three sensors, the streamwise coherence decays exponentially, similarly to Corcos' model for a fully turbulent flat-plate equilibrium boundary layer. In the experiments, at about 1–2 kHz, there is an additional hump. The latter also appears in the current computations, but shifted towards higher frequencies at around 4 kHz (solid and dashed circles found in Figs. 17(a) and 17(b)). As mentioned by Roger and Moreau [25], the increase in coherence values could be related to the vortex shedding caused by the laminar flow separation. Within this perspective, the shift towards higher frequencies in the DNS is most likely related to the changes in the LSB size with respect to the experimental case.

The evaluation of the streamwise coherence near the trailing edge shows a decreasing trend of the coherence with the increase in the distance between the sensors. Once again, there is an exponential decay up to 1 kHz and a small bump of correlated structures around 1 kHz. Moreau and Roger [27] also attributed the source of such a bump to some vortex shedding similar to the one caused by the laminar flow separation at the leading edge.

In all the above streamwise coherence, there is a mid-to-high frequency bump that is presumably related to vortex shedding. Such a vortex shedding mechanism should occur at a dominant Strouhal number between 0.2 and 0.3 given the present Reynolds number. At the trailing edge, even though there is no full separation of the mean flow, turbulent vortex shedding occurs inside the boundary layer, as evidenced in Fig. 5(b). Roger and Moreau [25] stated that vortex shedding occurs around a dominant frequency. They provided a Gaussian distribution on the logarithmic frequency scale formulation of the coherence between two spanwise sensors

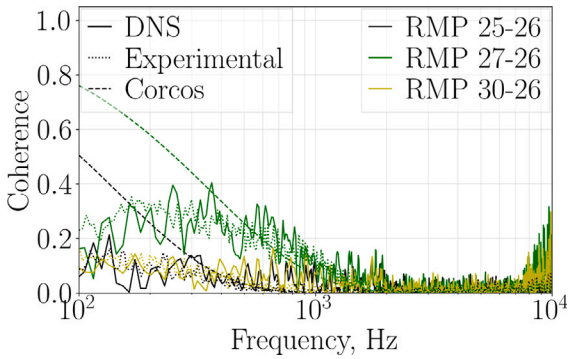

Fig. 16. Spanwise coherence at the aft positions on the suction side. Comparison with experimental data extracted from Moreau and Roger [27].

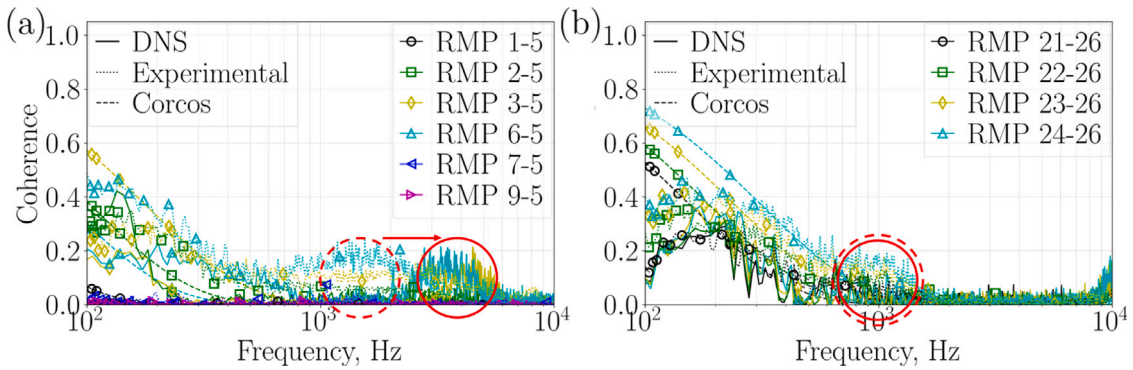

Fig. 17. Streamwise coherence at the front and aft positions on the suction side. References (a) RMP 5 and (b) RMP 26. Comparison with experimental data extracted from Moreau and Roger [27] and Corcos' model [58]. Solid and dashed ellipses and circles stressing the exponential decay and hump in the DNS and experimental results, respectively.

as

$$\gamma^2(\eta_z, f) = e^{\left(-\frac{|\eta_z|}{0.0025}\right)} e^{\left\{-75\left(\frac{\log_{10}(f^*) - \log_{10}(f_0^*)}{\log_{10}(f_0^*)}\right)^2\right\}} \tag{21}$$

with η_z the spanwise separation, the dimensionless frequency $f^* = f/(1\text{ Hz})$, and $f_0^* = f_0/(1\text{ Hz})$, with $f_0 = 0.22\,U_0/\delta$, where U_0 is the flow field velocity and δ is the local boundary layer thickness as the latter was used in the experiments at ECL [25]. In the current simulation $\delta/c = 6.6\times10^{-3}$ at the location of RMP 3 and $\delta/c = 4.75\times10^{-2}$ at RMP 26. This model has been applied to RMP 26 and RMP 3 (Figs. 18(a) and 18(b), respectively), to evaluate the spanwise coherence in both airfoil regions. The coherence model is compared to the DNS results at the same separation distance between sensors. Near the trailing edge, a nice match is observed for all separations, with a peak at $St \approx 0.2-0.3$ indicating dominant vortex shedding. Near the leading edge, within the LSB, the results do not collapse as smoothly as in Fig. 18(a), as there are presumably two mechanisms (bi-modal distribution): at low frequencies, the LSB breathing and around $St \approx 0.2-0.3$ the vortex shedding.

The evaluation of the streamwise coherence has then been carried out in the LSB. The process is analogous to the previous spanwise coherence. The formulation of Roger and Moreau (Eq. (21)) has been modified as follows:

$$\gamma^2(\eta_x, f) = 1.25e^{\left(-\frac{|\eta_x|}{0.0035}\right)} e^{\left\{-450\left(\frac{\log_{10}(f^*) - \log_{10}(f_0^*)}{\log_{10}(f_0^*)}\right)^2\right\}} \tag{22}$$

with η_x the streamwise separation, the dimensionless frequency $f^* = f/(1\text{ Hz})$, and $f_0^* = f_0/(1\text{ Hz})$, with $f_0 = 0.27U_0/\delta$, where U_0 and δ are the local edge velocity and boundary layer thickness at RMP 3. Fig. 19(a) shows the mean and instantaneous flow behavior at the LSB, with an emphasis on the location of RMP 3. The flow does not evolve in the same manner on both sides of the probe. In the front part of the LSB the flow is laminar and steady (calm region), whereas in the rear part a strong vortex shedding occurs yielding a large mean reverse-flow zone. Therefore, both behaviors have been represented separately in Figs. 19(b) and 19(c) respectively. The sudden drop in coherence in Fig. 19(b) at Strouhal numbers greater than 0.3 can be related to the steady laminar region and the lack of small turbulent structures. Both, the frequency at which the maximum coherence is found in the hump centered around Strouhal numbers 0.23–0.27, and the ratio of decay with distance are matching the DNS results, and that of Malmir et al. [59] at high frequencies ($St_\delta = 0.25$). The additional hump centered around Strouhal numbers 0.01–0.012 also corresponds to the low-frequency mechanism (aforementioned LSB breathing) found by Malmir et al. [59] ($St_\delta = 0.012$). Finally, the streamwise coherence between RMPs 3 and 5 (which are located 4.3 mm apart) is isolated, and represented in Fig. 20, together with the spanwise coherence at the trailing edge, for probes 3 mm apart. The results are compared with the corresponding model and experimental data of Roger and Moreau [25]. For all cases in both streamwise and spanwise directions, the location of the maximum coherence is found at about $St \approx 0.2-0.3$, which confirms the significant vortex shedding that occurs at both the LSB and the trailing edge, and the correlation of the flow mechanisms on the suction side. In summary, a previous experimental conjecture on the similar vortex shedding contribution of the laminar separation bubble and the turbulent eddies near the airfoil trailing edge is confirmed numerically for the first time, and those coherent structures responsible for vortex shedding most likely explain the humps seen in the PSD of wall-pressure fluctuations on both airfoil sides. This could yield two separate noise sources that contribute at high frequencies beyond 4–5 kHz.

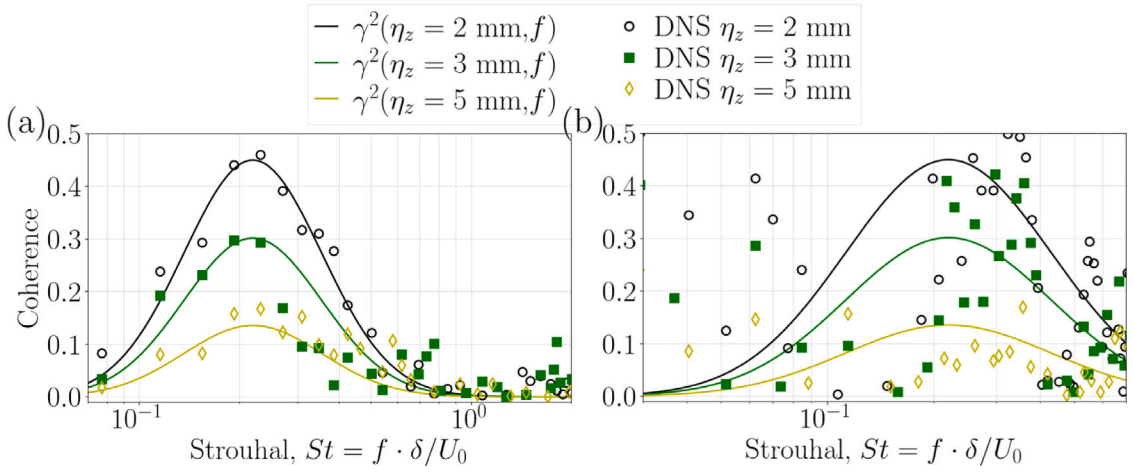

Fig. 18. Reduced spanwise coherence. (a) trailing edge around RMP 26, and (b) leading edge around RMP 3. Strouhal number based on local boundary layer thickness.

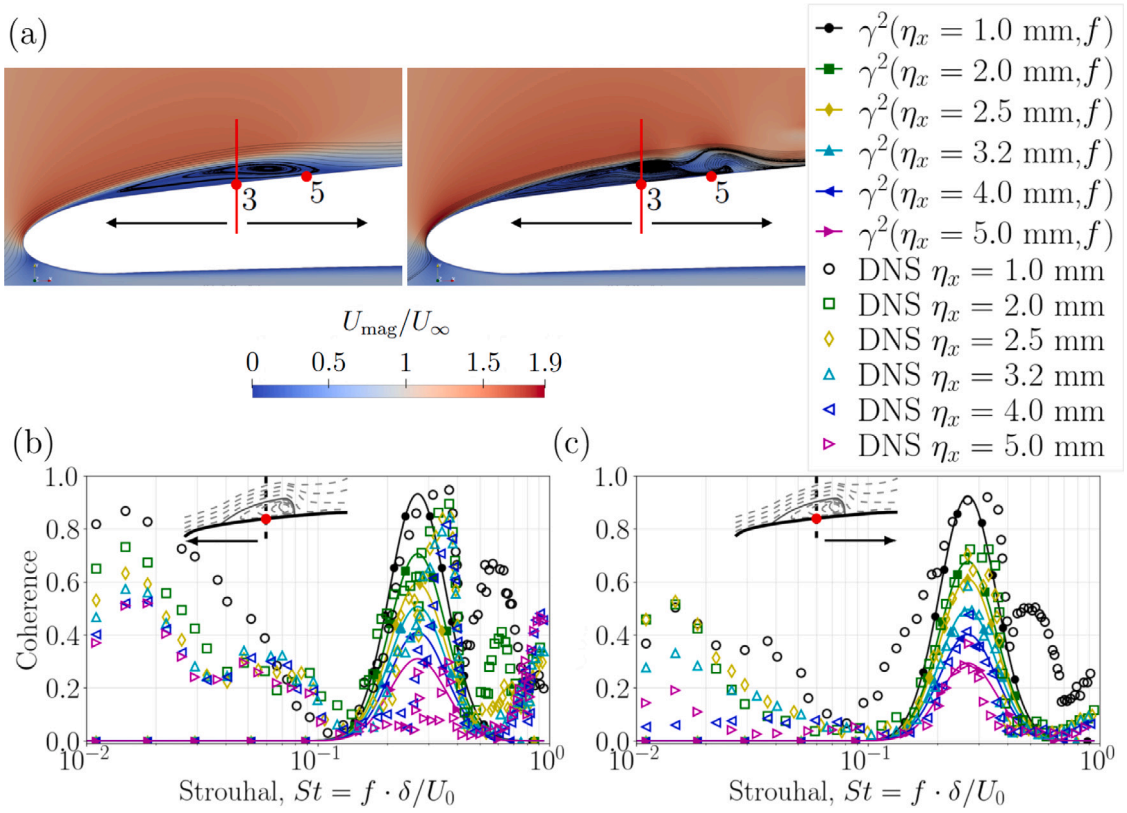

Fig. 19. (a) Boundary layer laminar separation bubble flow. Mean (left) and instantaneous (right) flow field. Reduced streamwise coherence around RMP 3; (b) sweep towards leading edge, (c) sweep towards trailing edge. Strouhal number based on local boundary layer thickness and edge velocity.

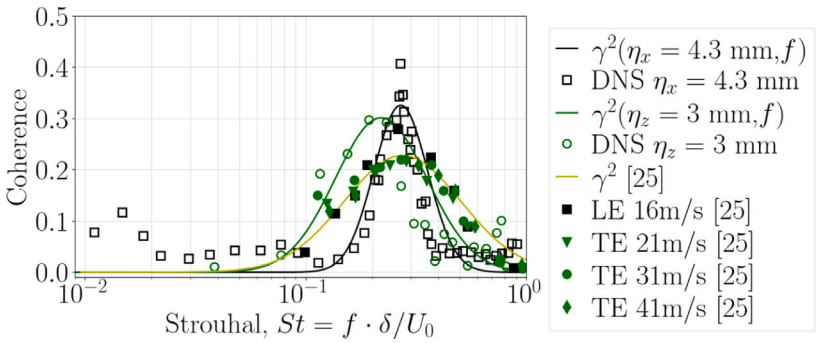

Fig. 20. Reduced streamwise and spanwise coherence with reference to RMPs 3 and 26 respectively. Current model and data compared to Roger and Moreau [25] model and experiment. Open symbols –DNS– and solid symbols –Roger and Moreau [25]–; square markers correspond to streamwise leading edge coherence, whereas other forms markers stand for spanwise trailing edge coherence.

3.4. Near and far field acoustic propagation

3.4.1. Dilatation field

In Fig. 21, the instantaneous contours of the Q-criterion colored by the velocity magnitude are superimposed on the dilatation field. The latter is computed as $-\partial\rho/\partial t$ and exhibits the noise sources near the airfoil [23]. As it depends only on the temporal resolution, it can be evaluated at various frequency ranges by band-pass filtering the desired range of frequency. The low-frequency, high-frequency and unfiltered field are therefore evaluated separately. The low frequency regime in Fig. 21(a) has a main noise source at the trailing edge, and a secondary contribution at the LSB. The efficiency of the latter is about ten times lower than that of the trailing-edge source in this frequency range, and is due to the laminar flow initial breakdown [60].

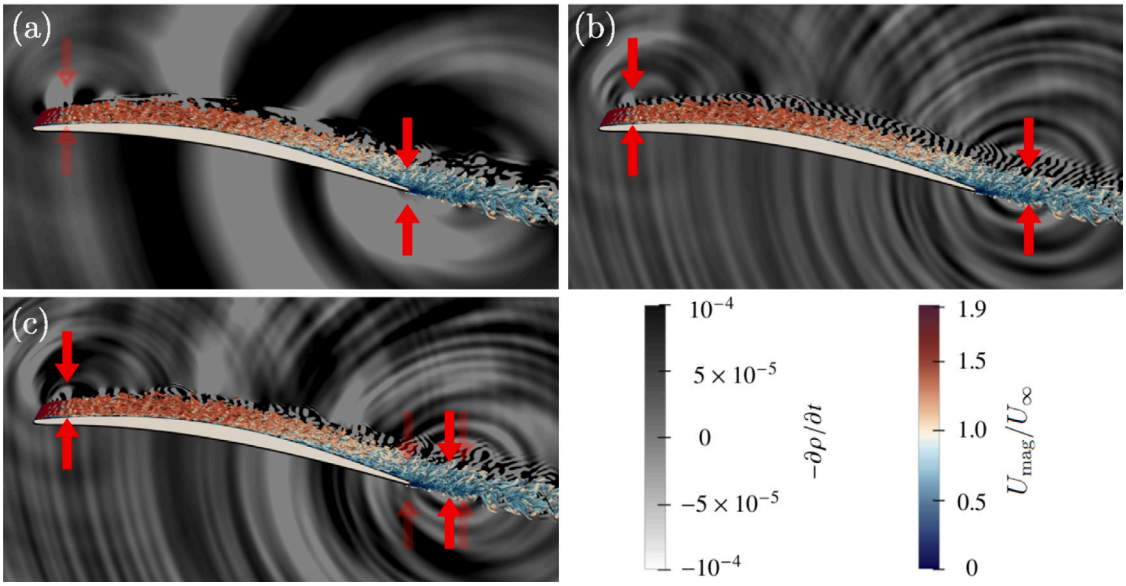

Fig. 21. Instantaneous field of Q-criterion velocity magnitude superimposed on the dilatation field contours $-\partial\rho/\partial t$. Filtering at various frequency ranges. (a) Low-frequencies filtering (1–1000 Hz), (b) High-frequencies filtering (5–15 kHz), and (c) No frequency filtering. Arrows pointing at the sound sources positions.

In the high-frequency range of Fig. 21(b), two noise sources are found. The LSB source, now more significant than in the low-frequency range, and a wake source. This near-wake source was first assessed by Wu et al. [23], and is now confirmed. Wu et al. [23] located it at a distance of $0.3\,c$ downstream the trailing edge, whereas here it is found about $0.2\,c$ downstream the trailing edge. It is located beyond the overlapping region of the O-grid and the background meshes. Globally, in the unfiltered dilatation field in Fig. 21(c), the combination of all noise sources is obtained. The effect of the LSB is clearly visible. Then, there is a combination of the trailing-edge source together with the near-wake producing elliptical wave fronts, which makes the rear of the airfoil a critical noise emitter. In summary, there are three main noise sources: the laminar separation bubble, the turbulent eddies near the trailing edge, and a third wake source downstream the trailing edge. Finally, in all three figures, the pseudo-sound generated by the wall flow eddies can also be distinguished as it vanishes within a short distance from the foil surface.

3.4.2. Far field prediction

The noise spectrum away from the trailing edge at 90° to the flow direction is shown in Fig. 22 for two distances: 1.21 m and 2 m. The predicted data (Amiet and FWH solid formulation) compare successfully with experimental and previous numerical data, stressing the proper noise decay with distance. Amiet's model is employed with both the direct wall-pressure spectrum at RMP 26, and the application of Lee's wall-pressure model with the DNS boundary-layer parameters.

The FWH prediction shows good agreement with the experimental data at low to mid frequencies. At 1.21 m, the current DNS result presents a drop at high frequencies instead of the plateau obtained in UdeS measurements and the solid formulation of FWH by

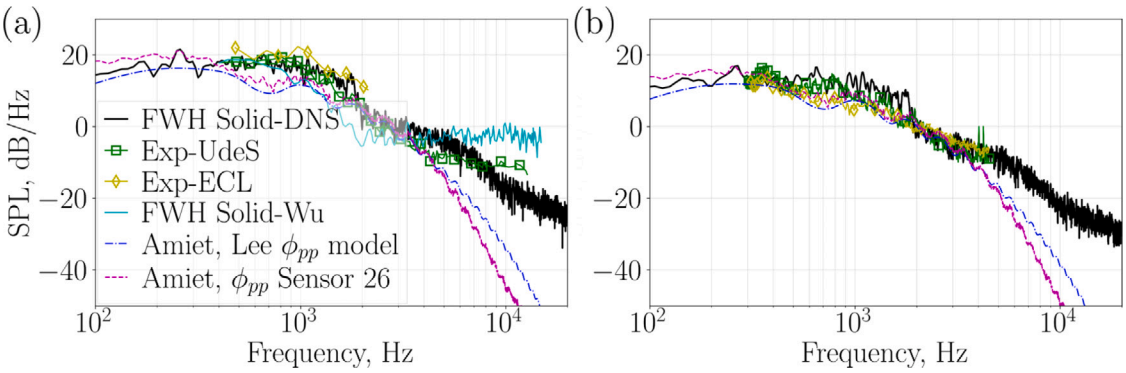

Fig. 22. Sound pressure level of far field noise propagation. (a) distance 1.21 m and (b) distance 2 m.

Wu et al. [23]. The latter related the plateau to the near wake noise source evidenced in Fig. 21, which might imply that the current DNS underestimates this additional noise source compared to Wu's simulation. Note that this is consistent with the wall-pressure predictions near the trailing edge (Figs. 12(g) and 12(h)). Amiet's theory, applied with the wall-pressure spectrum at the trailing edge (RMP 26), provides a good prediction of noise levels up to 4 kHz. When it is applied with the wall-pressure spectrum provided by Lee's model, there is a slight underprediction of the noise levels. This is again caused by the lower sound pressure level in this same frequency range found in Fig. 12(h). At high frequencies, Amiet produces a faster decay ratio of the sound pressure levels than the FWH counterpart, and the experimental data. When using Lee's WPS model, this ratio of decay is slightly lower, as the corresponding SPL at the wall also decays slower. The departure of the FWH predictions from those obtained with Amiet's model beyond $4-5$ kHz also confirms that the main trailing-edge scattering is no longer the dominant source in the high-frequency range, confirming quantitatively the observations made on the filtered dilatation field.

3.4.3. Directivity

Finally, the single-frequency directivity is shown in Fig. 23 for multiple distances to the trailing edge. At low frequencies (Helmholtz numbers $kc < 1$, where $k = 2\pi f/c_0$ denotes the acoustic wave number, f the frequency, and c_0 the speed of sound in the surrounding medium), the directivity corresponds to a compact dipolar distribution with its characteristic symmetrical lobe pattern aligned with the airfoil. As the frequency increases, the source becomes non-compact (as shown by the additional lobes) and the possible effect of quadrupolar sources turns out to be more and more important. Progressively, the lobes of the directivity are more and more tilted towards the downstream direction. This tilting is represented by the curved arrows that increase in width in Figs. 23(d)–23(f). It is caused by the dominant LSB noise source diffracting at the leading edge. Moreover, extra lobes appear from $kc = 4\pi$ on the suction side. The higher frequency, the more lobes are seen, as represented by the diagonal arrows in Figs. 23(e) and 23(f). These lobes are related to the near-wake noise source evidenced in Fig. 21. Similarly, the noise propagation gets a preferential direction towards the flow downstream and its center of propagation shifts to the wake, as represented by the horizontal double-sided arrow. This preference for downstream propagation is linked to the combined effect of the LSB sources near the leading edge and the additional wake source. This is also consistent with Fig. 17(a) showing a high coherence in the LSB in this high frequency range, pointing to a leading noise source and a noise radiation more towards the trailing edge.

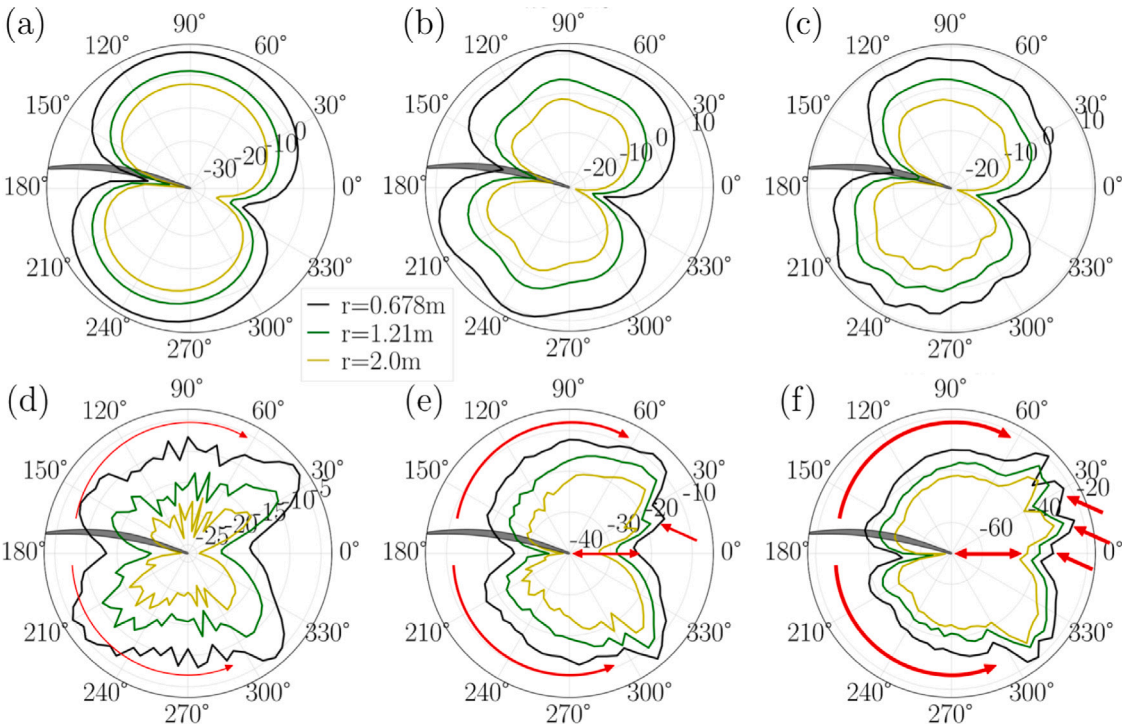

Fig. 23. Single-frequency directivity on far field at several distances from the trailing edge. Helmholtz numbers: (a) $kc = 0.3$, (b) $kc = 1.5$, (c) $kc = \pi$, (d) $kc = 2\pi$, (e) $kc = 4\pi$, and (f) $kc = 16\pi$. Sound Pressure Level (SPL), dB/Hz. The curved arrows represent the tilting of the lobular pattern towards the trailing edge. Their increase in thickness represents the increased tiling effect. The diagonal arrows point at additional lobes, and the double-sided horizontal arrows show the shift of the downstream propagation center.

4. Conclusion

A compressible Direct Numerical Simulation of a Controlled Diffusion airfoil at 8° in a jet flow at $Re = 1.5 \times 10^5$, replicating open-jet experimental conditions, has been carried out. A novel overlapping mesh topology is employed, allowing flexible angle of attack modifications without remeshing. The DNS is validated against experimental data and a previous DNS that used a different meshing strategy.

Detailed mean flow results and wall-pressure statistics performed on both suction and pressure sides for the first time reveal (i) a laminar separation bubble on the suction side, inducing turbulent flow transition, and producing a hump in noise levels in the mid-frequency range, (ii) a vortex shedding at the trailing edge, (iii) a near-wake source, and finally (iv) mid-frequency quasi-tonal humps linked to upstream-propagating acoustic waves on the pressure side. The latter is confirmed by two-point space–time correlation of the fluctuating pressure, showing disturbances propagating at the speed of sound over the whole pressure side. Moreover, coherence of wall-pressure fluctuations in both streamwise and spanwise directions not only exhibit an exponential decay at low frequencies, but also an additional hump at mid-to-high frequencies near the leading and trailing edges. A detailed analysis of this mid-to-high frequency hump confirms a previous experimental conjecture that a similar vortex shedding mechanism dominates the leading-edge LSB and the turbulent boundary layer near the trailing edge.

Discrepancies with experiments and a previous DNS, primarily in LSB size and external velocity field, are linked to the absence of turbulence injection and where the boundary conditions were imposed, which affects wall-pressure spectra and coherence. Nevertheless, the current DNS nicely captures the main low-to-mid frequency levels, but does not capture the full roll-off at higher frequencies.

Dilatation contours and directivity plots confirm the presence of three main noise sources: (i) the flow separation and reattachment at the leading edge on the suction side, producing a LSB; (ii) the interaction between the attached turbulent flow and the airfoil suction side at the trailing edge; (iii) a noise source in the near wake, located close to the trailing edge. Far-field noise predictions using Ffowcs Williams and Hawkings analogy show good agreement with experimental data at low-to-mid frequencies, but a faster decay is observed at high frequencies, likely due to the weaker near-wake source. Amiet's analogy also provides good agreement with FWH and experiment up to 4 kHz, but fails to capture the high-frequency plateau. Since Amiet's analogy only relies on the trailing edge wall-pressure spectrum, it suggests that this high-frequency range is dominated by the LSB and near-wake sources. Finally, the directivity patterns reveal a transition from a symmetric compact dipole at low-frequencies, to non-compact multi-lobed structures at higher frequencies because of the near-wake and the LSB sources. The latter is also responsible for the tilting in the directivity pattern towards downstream.

In summary, this work provides new insights into airfoil self-noise generation mechanisms, emphasizing the key role of LSB and vortex shedding at the trailing edge. This study also confirms the previous conjecture on the significance of the near-wake contributions at high frequencies, as well as the presence of acoustic waves propagating upstream over the whole airfoil, suggesting potential interactions with the jet, due to installation effects.

CRediT authorship contribution statement

Andrea Arroyo Ramo: Writing – review & editing, Writing – original draft, Visualization, Validation, Software, Methodology, Investigation, Formal analysis, Data curation, Conceptualization. **Stéphane Moreau:** Writing – review & editing, Supervision, Resources, Project administration, Methodology, Funding acquisition, Formal analysis, Conceptualization. **Richard D. Sandberg:** Writing – review & editing, Software. **Michaël Bauerheim:** Writing – review & editing, Supervision, Resources, Project administration, Methodology, Funding acquisition, Formal analysis, Conceptualization. **Marc C. Jacob:** Writing – review & editing, Methodology.

Funding sources

This work was partially supported by the French "Programme d'Investissements d'avenir", conducted by the ARN-"Agence nationale de la recherche" through the EUR-TSAE scholarship. The authors also acknowledge the support of the Natural Sciences and Engineering Research Council of Canada (NSERC) through the Discovery grant.

Declaration of competing interest

The authors declare that they have no known competing financial interests or personal relationships that could have appeared to influence the work reported in this paper.

Acknowledgments

This research was carried out with the assistance of resources and services from the Digital Research Alliance of Canada and the National Computational Infrastructure (NCI), which is supported by the Australian Government. The authors would like to acknowledge Dr. Hao Wu for DNS data, and Dr. Pawel Przytarski, Dr. Massimiliano Nardini, and Dr. Richard Pichler for their support and assistance in the use of *HiPSTAR*.

Appendix. Comparison with wu's DNS

The differences between the two Navier–Stokes DNS in the present study can be mostly traced to how installation effects in anechoic open-jet wind tunnels are accounted for.

In both DNS, a prior 2D RANS simulation of the complete experimental setup is used to provide the steady boundary conditions found in the wind tunnel [3] on reduced domains on which the DNS are performed. The first discrepancy between the two DNS is due to the use of RANS simulations with different mesh topologies and grid refinements, in addition to small differences in the computational domains shown in Fig. A.1(a). Hence, the mean flow field used as initialization and boundary conditions in each DNS differs. Moreover, the DNS embed unsteady turbulent effects not present in the RANS simulations: as the reduced computational domains shown by solid lines in Fig. A.1(b)) do not overlap to allow a Cartesian background mesh in the present DNS instead of the multiblock structured topology used by Wu et al. [24]. In the latter, the DNS domain is tailored to the jet deflection at 8°, while in the current DNS the jet shear-layer intersects the domain in the top right corner, due to Cartesian background constraints, as evidenced in Fig. 3.

To evaluate this effect induced by different reduced computational domains, initializations and steady boundary conditions, a set of lines close to the inlet, top and bottom boundaries of the current DNS computation (dotted black lines in Fig. A.1(b)) have been used to evaluate the local mean velocity profiles. The vertical and horizontal velocity profiles are represented in Figs. A.2 and A.3, respectively.

In general, the trends on the mean velocity profiles are similar in every simulation. However, there is a consistent shift in the values between the two DNS. Overall, there is a discrepancy lower than 5% in the horizontal component. Larger differences are found in the vertical velocity component similarly to what was already reported between the "Previous RANS" results and the hot-wire measurements performed at ECL (Figs. 11 and 12 in [61]). The larger variation in mean vertical velocity then induces differences in the flow deflection of the jet by the airfoil, and in the angle of attack seen by the airfoil. This is thought to be the main reason for the different laminar separation bubble sizes and consequently the different evolution of the turbulent boundary layer after transition. Note that in the actual experiment, the state of the jet itself at the nozzle exit also influences the incidence seen by the airfoil and the transition process on the airfoil, as recently shown in [62]. Notice that the DNS use the RANS computations as steady boundary conditions. Therefore, when comparing DNS with its associated RANS, as moving farther from the boundaries, larger discrepancies appear between them due to differences in the space–time solution between the simulations.

An additional effect of the jet is the acoustic and turbulent fluctuations that it produces in the potential core that will affect the transition process on the airfoil. For instance, as shown in Fig. A.2(b) (there is a sudden drop in the velocity components beyond $x/c = 1.1$), associated with the jet-shear layer occurring within the simulation (top right corner of the current DNS). This shear layer is found within the DNS domain. On the other hand, Wu's DNS is truly turbulence-free. Moreover, different inlet turbulence levels have also been reported upstream of the airfoil in [62] as a consequence of different jet shear-layer development.

Overall, the differences between the two DNS can be seen as the discrepancies that would be obtained while measuring the same experimental setup in two different wind-tunnels.

Data availability

Data will be made available on request.

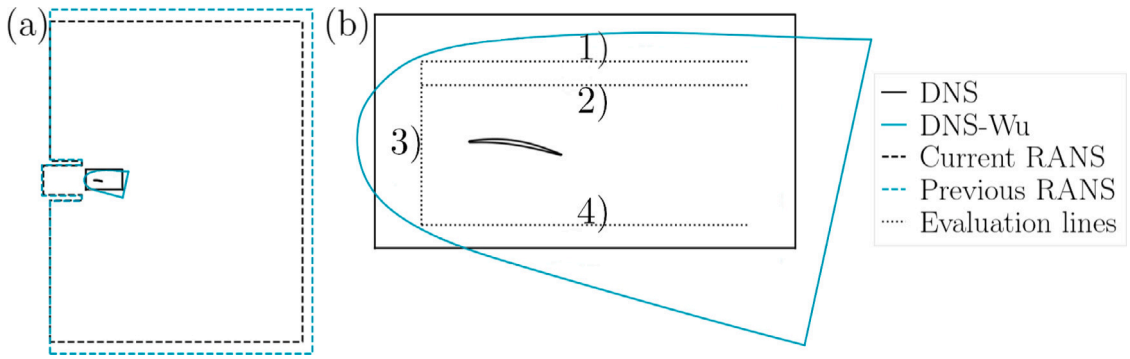

Fig. A.1. Mesh limits used in simulations. (a) Current and previous RANS complete experimental domain, (b) DNS domains and previous RANS reduced domains (current RANS reduced domain overlapping with DNS domain). Lines used to evaluate positions close to the boundary conditions. (1) upper-top, (2) top (two lines, one closer to the airfoil), (3) inlet, and (4) bottom.

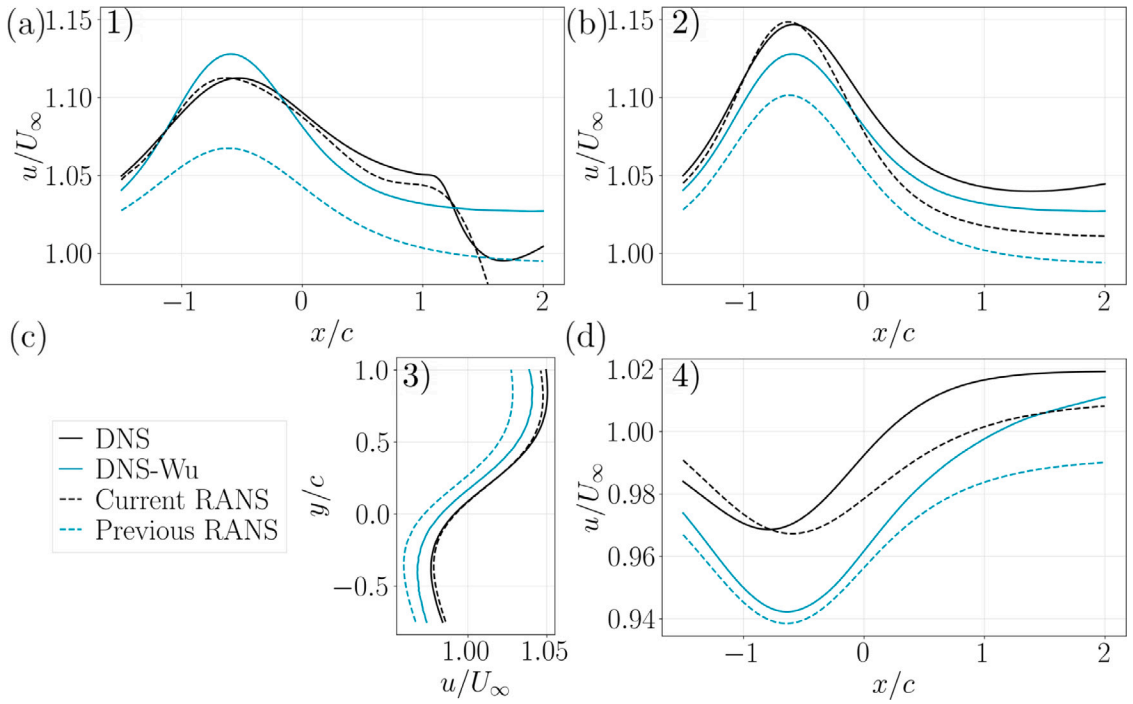

Fig. A.2. Horizontal mean velocity profiles. Comparison in the (a) upper-top (b) top (c) inlet, and (d) bottom lines found in Fig. A.1. Comparison of current DNS, Wu's DNS, previous RANS, and current RANS used as initialization and boundaries in the simulation.

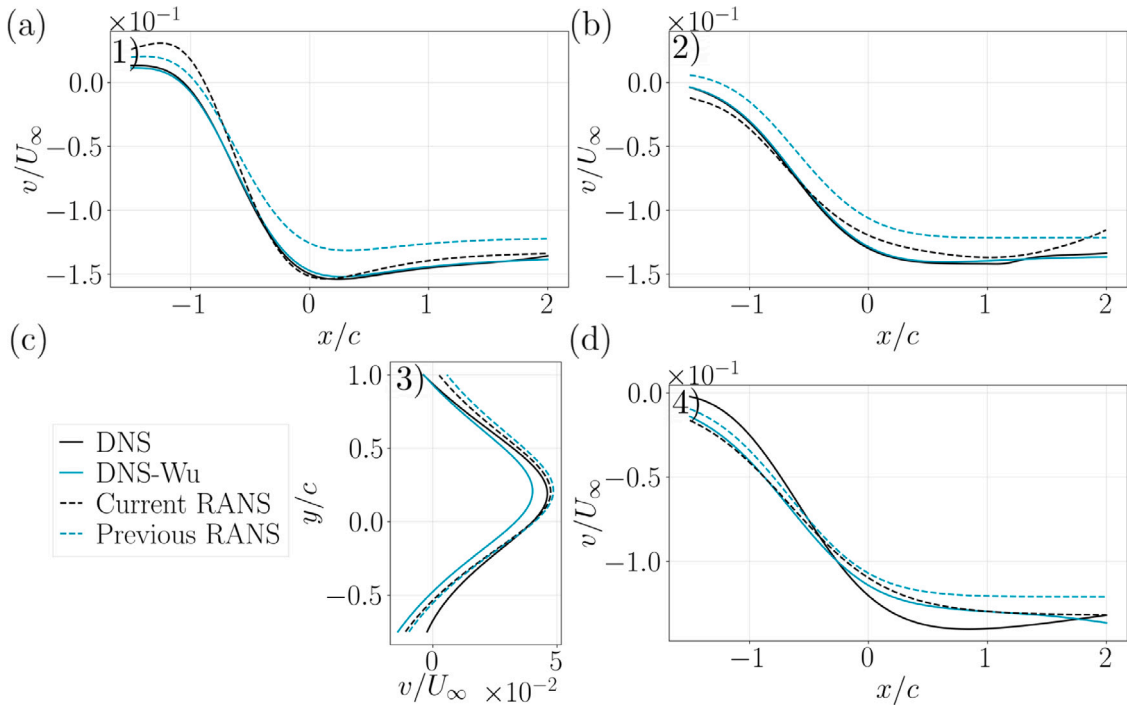

Fig. A.3. Vertical mean velocity profiles. Comparison in the (a) upper-top (b) top (c) inlet, and (d) bottom lines found in Fig. A.1. Comparison of current DNS, Wu's DNS, previous RANS, and current RANS used as initialization and boundaries in the simulation.

References

[1] S. Moreau, M. Roger, Competing broadband noise mechanisms in low-speed axial fans, AIAA J. 45 (1) (2007) 48–57, http://dx.doi.org/10.2514/1.14583.
[2] S. Moreau, Turbomachinery noise predictions: Present and future, MDPI Acoustics (1) (2019) 92–116, http://dx.doi.org/10.3390/acoustics1010008.
[3] S. Lee, L. Ayton, F. Bertagnolio, S. Moreau, T.P. Chong, P. Joseph, Turbulent boundary layer trailing-edge noise: Theory, computation, experiment, and application, Prog. Aerosp. Sci. 126 (June) (2021) 100737, http://dx.doi.org/10.1016/j.paerosci.2021.100737.
[4] T.F. Brooks, T.H. Hodgson, Trailing edge noise prediction from measured surface pressures, J. Sound Vib. 78 (1) (1981) 69–117, http://dx.doi.org/10.1016/S0022-460X(81)80158-7.
[5] R.D. Sandberg, L.E. Jones, N.D. Sandham, P.F. Joseph, Direct numerical simulations of tonal noise generated by laminar flow past airfoils, J. Sound Vib. 320 (1) (2009) 838–858, http://dx.doi.org/10.1016/j.jsv.2008.09.003.
[6] T. Padois, P. Laffay, A. Idier, S. Moreau, Tonal noise of a controlled-diffusion airfoil at low angle of attack and Reynolds number, J. Acoust. Soc. Am. 140 (1) (2016) http://dx.doi.org/10.1121/1.4958916.
[7] M. Sanjosé, A. Towne, P. Jaiswal, S. Moreau, S. Lele, Modal analysis of the laminar boundary layer instability and tonal noise of an airfoil at Reynolds number 150,000, Int. J. Aeroacoustics 18 (2–3) (2019) 317–350, http://dx.doi.org/10.1177/1475472X18812798.
[8] J.E. Ffowcs-Williams, L.H. Hall, Aerodynamic sound generation by turbulent flow in the vicinity of a scattering half plane, J. Fluid Mech. 40 (4) (1970) 657–670, http://dx.doi.org/10.1017/S0022112070000368.
[9] R.K. Amiet, Noise due to turbulent flow past a trailing edge, J. Sound Vib. 47 (3) (1976) 387–393, http://dx.doi.org/10.1016/0022-460X(76)90948-2.
[10] M.S. Howe, Theory of vortex sound, in: Cambridge Texts in Applied Mathematics, Cambridge University Press, 2003, p. 216, http://dx.doi.org/10.1017/CBO9780511755491.
[11] N. Curle, The influence of solid boundaries upon aerodynamic sound, Proc. R. Soc. Lond. A 231 (1187) (1955) 505–514, http://dx.doi.org/10.1098/rspa.1955.0191.
[12] R.K. Amiet, Acoustic radiation from an airfoil in a turbulent stream, J. Sound Vib. 41 (4) (1975) 407–420, http://dx.doi.org/10.1016/S0022-460X(75)80105-2.
[13] M. Roger, S. Moreau, Back-scattering correction and further extensions of Amiet's trailing-edge noise model. Part 1: theory, J. Sound Vib. 286 (3) (2005) 477–506, http://dx.doi.org/10.1016/j.jsv.2004.10.054.
[14] S. Moreau, M. Roger, Back-scattering correction and further extensions of Amiet's trailing-edge noise model. Part II: Application, J. Sound Vib. 323 (1) (2009) 397–425, http://dx.doi.org/10.1016/j.jsv.2008.11.051.
[15] M. Roger, S. Moreau, Addendum to the back-scattering correction of Amiet's trailing-edge noise model, J. Sound Vib. 331 (24) (2012) 5383–5385, http://dx.doi.org/10.1016/j.jsv.2012.06.019.
[16] W.R. Wolf, J.L. Azevedo, S.K. Lele, Convective effects and the role of quadrupole sources for aerofoil aeroacoustics, J. Fluid Mech. 708 (2012) 502–538, http://dx.doi.org/10.1017/jfm.2012.327.
[17] J. Winkler, H. Wu, S. Moreau, T. Carolus, R.D. Sandberg, Trailing-edge broadband noise prediction of an airfoil with boundary-layer tripping, J. Sound Vib. 482 (2020) 115450:1–25, http://dx.doi.org/10.1016/j.jsv.2020.115450.
[18] M. Deuse, R.D. Sandberg, Different noise generation mechanisms of a controlled diffusion aerofoil and their dependence on mach number, J. Sound Vib. 476 (2020) 115317, http://dx.doi.org/10.1016/j.jsv.2020.115317.
[19] R.D. Sandberg, N.D. Sandham, P.F. Joseph, Direct numerical simulations of trailing-edge noise generated by boundary-layer instabilities, J. Sound Vib. 304 (3) (2007) 677–690, http://dx.doi.org/10.1016/j.jsv.2007.03.011.
[20] R.D. Sandberg, N.D. Sandham, Direct numerical simulation of turbulent flow past a trailing edge and the associated noise generation, J. Fluid Mech. 596 (2008) 353–385, http://dx.doi.org/10.1017/S0022112007009561.
[21] M. Sanjosé, S. Moreau, M.S. Kim, F. Pérot, Direct self-noise simulation of the installed controlled diffusion airfoil, in: Proceedings of the 17th AIAA/CEAS Aeroacoustics Conference (32nd AIAA Aeroacoustics Conference), in: 2011-2716, 25-29 June, Portland, Oregon, USA, 2011, http://dx.doi.org/10.2514/6.2011-2716.
[22] H. Wu, S. Moreau, R. Sandberg, Effects of pressure gradient on the evolution of velocity-gradient tensor invariant dynamics on a controlled-diffusion aerofoil at $Re_c = 150000$, J. Fluid Mech. 868 (2019) 584–610, http://dx.doi.org/10.1017/jfm.2019.129.
[23] H. Wu, S. Moreau, R. Sandberg, On the noise generated by a controlled-diffusion aerofoil at $Re_c = 1.5 \times 10^5$, J. Sound Vib. 487 (2020) 116152: 1–20, http://dx.doi.org/10.1016/j.jsv.2020.115620.
[24] H. Wu, R. Sandberg, S. Moreau, Stability characteristics of different aerofoil flows at $Re_c = 1.5 \times 10^5$ and the implications for aerofoil self-noise, J. Sound Vib. 506 (2021) 115620: 1–25, http://dx.doi.org/10.1016/j.jsv.2021.116152.
[25] M. Roger, S. Moreau, Broadband self-noise from loaded fan blades, AIAA J. 42 (3) (2004) 536–544, http://dx.doi.org/10.2514/1.9108.
[26] S. Moreau, G. Iaccarino, S. Kang, Y. Khalighi, M. Wang, Numerical simulation of a low speed fan blade, in: Proceedings of the CTR Summer Program, 25-29 June, Stanford, California, USA, 2004, pp. 195–207.
[27] S. Moreau, M. Roger, Effect of airfoil aerodynamic loading on trailing-edge noise sources, AIAA J. 43 (1) (2005) 41–52, http://dx.doi.org/10.2514/1.5578.
[28] M. Wang, S. Moreau, G. Iaccarino, M. Roger, LES prediction of wall-pressure fluctuations and noise of a low-speed airfoil, Int. J. Aeroacoustics 8 (3) (2009) 177–198, http://dx.doi.org/10.1121/1.2934513.
[29] P. Jaiswal, S. Moreau, F. Avallone, D. Ragni, S. Pröbsting, On the use of two-point velocity correlation in wall-pressure models for turbulent flow past a trailing edge under adverse pressure gradient, Phys. Fluids 32 (10) (2020) 105105 1–27, http://dx.doi.org/10.1063/5.0021121.
[30] R. Boukharfane, M. Parsani, J. Bodart, Characterization of pressure fluctuations within a controlled-diffusion blade boundary layer using the equilibrium wall-modelled LES, Sci. Rep. 10 (1) (2020) 1–19, http://dx.doi.org/10.1038/s41598-020-69671-y.
[31] R. Boukharfane, T. Bridel-Bertomeu, J. Bodart, L. Joly, M.C. Jacob, Characterization of the pressure fluctuations within a controlled-diffusion airfoil boundary layer at large Reynolds numbers, in: 25th AIAA/CEAS Aeroacoustics Conference, 2019, pp. 1–17, http://dx.doi.org/10.2514/6.2019-2722.
[32] P. Jaiswal, Y. Pasco, G. Yakhina, S. Moreau, Experimental investigation of aerofoil tonal noise at low mach number, J. Fluid Mech. 932 (2022) A37:1–31, http://dx.doi.org/10.1017/jfm.2021.1018.
[33] S. Moreau, M. Henner, G. Iaccarino, M. Wang, M. Roger, Analysis of flow conditions in freejet experiments for studying airfoil self-noise, AIAA J. 41 (10) (2003) 1895–1905, http://dx.doi.org/10.2514/2.1905.
[34] J. Winkler, S. Moreau, T. Carolus, Airfoil trailing-edge blowing: Broadband noise prediction from large-eddy simulation, AIAA J. 50 (2) (2012) 294–303, http://dx.doi.org/10.2514/1.J050959.
[35] J. Christophe, J. Anthoine, S. Moreau, Trailing edge noise of a controlled-diffusion airfoil at moderate and high angle of attack, in: Proceedings of the 15th AIAA/CEAS Aeroacoustics Conference, in: 2009-3196, 11-13 May, Miami, Florida, USA, 2009, http://dx.doi.org/10.2514/6.2009-3196.
[36] S. Moreau, M. Roger, J. Christophe, Flow features and self-noise of airfoils near stall or in stall, in: Proceedings of the 15th AIAA/CEAS Aeroacoustics Conference, (2009–3198) 11-13 May, Miami, Florida, USA, 2009, pp. 1–20, http://dx.doi.org/10.2514/6.2009-3198.
[37] R.D. Sandberg, Compressible-flow DNS with application to airfoil noise, FTaC 95 (2015) 211–229, http://dx.doi.org/10.1007/s10494-015-9617-1.
[38] M. Deuse, High-Fidelity Numerical Investigation of Different Mechanisms of Aerofoil Self-Noise (Master's thesis), Department of Mechanical Engineering, The University of Melbourne, 2020, URL https://hdl.handle.net/11343/238524.

[39] M.H. Carpenter, D. Gottlieb, S. Abarnanel, Stable and accurate boundary treatments for compact, high-order finite-difference schemes, Appl. Numer. Math. 12 (1993) 55–87, http://dx.doi.org/10.1016/0168-9274(93)90112-5.
[40] M. Deuse, R.D. Sandberg, Implementation of a stable high-order overset grid method for high-fidelity simulations, Comput. & Fluids 211 (2020) http://dx.doi.org/10.1016/j.compfluid.2020.104449.
[41] A. Arroyo Ramo, S. Moreau, R.D. Sandberg, M. Bauerheim, M.C. Jacob, Direct numerical simulation of controlled diffusion airfoil, in: Proceedings of the 28th AIAA/CEAS Aeroacoustics Conference, in: 2022-2815, 14-17 June, Southampton, UK, 2022, http://dx.doi.org/10.2514/6.2022-2815.
[42] S.B. Pope, Turbulent Flows, Cambridge University Press, Cambridge, 2000, p. 807, http://dx.doi.org/10.1017/CBO9780511840531.
[43] H.S.K. Gersten, Boundary-Layer Theory, Springer Nature, 2000, p. 814, http://dx.doi.org/10.1007/978-3-662-52919-5, Ninth edition.
[44] C.A. Kennedy, M.H. Carpenter, R.M. Lewis, Low-storage, explicit Runge–Kutta schemes for the compressible Navier–Stokes equationss, Appl. Numer. Math. 35 (2000) 177–219, http://dx.doi.org/10.1016/S0168-9274(99)00141-5.
[45] R.D. Sandberg, N.D. Sandham, Nonreflecting zonal characteristic boundary condition for direct numerical simulation of aerodynamic sound, AIAA J. 44 (2) (2006) 402–405, http://dx.doi.org/10.2514/1.19169.
[46] A. Arroyo Ramo, S. Moreau, R.D. Sandberg, M. Bauerheim, M.C. Jacob, Controlled diffusion airfoil self-noise, an acoustic far-field prediction, in: Proceedings of the AIAA Aviation 2023 Forum, in: 2023-3505, 12-16 June, San Diego, California, USA, 2023, http://dx.doi.org/10.2514/6.2023-3505.
[47] S. Lee, Empirical wall-pressure spectral modeling for zero and adverse pressure gradient flows, AIAA J. 56 (2018) 1–12, http://dx.doi.org/10.2514/1.J056528.
[48] Y. Rozenber, G. Robert, S. Moreau, Wall-pressure spectral model including the adverse pressure gradient effects, AIAA J. 50 (10) (2012) 2168–2179, http://dx.doi.org/10.2514/1.J051500.
[49] D. Höwer, Unsteady Pressure Fluctuations on the Surface of a Controlled Diffusion Airfoil (Master's thesis), Department of Mechanical Engineering, RWTH University, 2012.
[50] H. Wu, M. Sanjosé, S.M. Stéphane, R.D. Sandberg, Direct numerical simulation of the self-noise radiated by the installed controlled-diffusion airfoil at transitional Reynolds number, in: Proceedings of the 18th AIAA/CEAS Aeroacoustics Conference, in: 2018-3797, 25-29 June, Atlanta, Georgia, USA, 2018, http://dx.doi.org/10.2514/6.2018-3797.
[51] M.S. Istvan, J.W. Kurelek, S. Yarusevych, Turbulence intensity effects on laminar separation bubbles formed over an airfoil, AIAA J. 56 (4) (2018) 1305–1710, http://dx.doi.org/10.2514/1.J056453.
[52] H. Wu, Direct Numerical Simulation of Airfoil Self-Noise at High Reynolds Numbers (Ph.D. thesis), Department of Mechanical Engineering, Université de Sherbrooke, 2019, URL http://hdl.handle.net/11143/15114.
[53] K.P. Griffin, L. Fu, P. Moin, General method for determining the boundary layer thickness in nonequilibrium flows, Phys. Rev. Fluids 6 (2021) 024608, http://dx.doi.org/10.1103/PhysRevFluids.6.024608.
[54] A. Caiazzo, S. Pargal, H. Wu, M. Sanjosé, J. Yuan, S. Moreau, On the effect of adverse pressure gradients on wall-pressure statistics in a controlled-diffusion aerofoil turbulent boundary layer, J. Fluid Mech. 960 (2023) A17, http://dx.doi.org/10.1017/jfm.2023.157.
[55] J.Y. Parlange, R.D. Braddock, G. Sander, Analytical approximations to the solution of the Blasius equation, Acta Mech. 38 (1) (1981) 119–125, http://dx.doi.org/10.1007/BF01351467.
[56] Y. Na, P. Moin, The structure of wall-pressure fluctuations in turbulent boundary layers with adverse pressure gradient and separation, J. Fluid Mech. 377 (1998) 347–373, http://dx.doi.org/10.1017/S0022112098003218.
[57] H.H. Schloemer, Effects of pressure gradients on turbulent-boundary-layer wall-pressure fluctuations, J. Acoust. Soc. Am. 42 (1) (1967) 93–113, http://dx.doi.org/10.1121/1.1910581.
[58] G.M. Corcos, The structure of the turbulent pressure field in boundary-layer flows, J. Fluid Mech. 18 (3) (1964) 353–378, http://dx.doi.org/10.1017/S002211206400026X.
[59] F. Malmir, G. Di Labbio, A. Le Floc'h, L. Dufresne, J. Weiss, J. Vétel, Low-frequency unsteadiness in laminar separation bubbles, J. Fluid Mech. 999 (2024) http://dx.doi.org/10.1017/jfm.2024.962.
[60] B. Greschner, J. Grilliat, M.C. Jacob, F. Thiele, Measurements and wall modeled LES simulation of trailing edge noise caused by a turbulent boundary layer, Int. J. Aeroacoustics 9 (3) (2010) 329–355, http://dx.doi.org/10.1260/1475-472X.9.3.329.
[61] S. Moreau, D. Neal, J. Foss, Hot-wire measurements around a controlled diffusion airfoil in an open-jet anechoic wind tunnel, J. Fluids Eng. 128 (4) (2006) 699–706, http://dx.doi.org/10.1115/1.2201644.
[62] Z. Zhou, S. Moreau, M. Sanjosé, Installation effects on airfoil self-noise estimated by direct numerical simulations, J. Sound Vib. 604 (2025) 118978, http://dx.doi.org/10.1016/j.jsv.2025.118978.